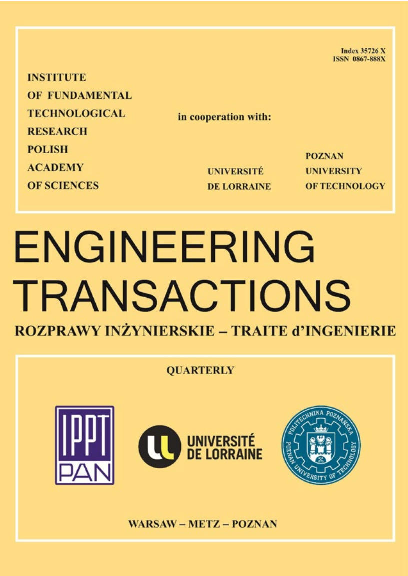

Index 35726 X
ISSN 0867-888X

INSTITUTE
OF FUNDAMENTAL
TECHNOLOGICAL
RESEARCH
POLISH
ACADEMY
OF SCIENCES

in cooperation with:

UNIVERSITÉ
DE LORRAINE

POZNAN
UNIVERSITY
OF TECHNOLOGY

ENGINEERING
TRANSACTIONS

ROZPRAWY INŻYNIERSKIE – TRAITE d'INGENIERIE

QUARTERLY

WARSAW – METZ – POZNAN

Title: Numerical Finite Element Modeling of Lamb Wave-Defect Interactions in Bonded Metal Structures: Benchmarking Mode Selection Criteria

Author(s): Ayoub Jabiri, Mustapha Azkour, Abdelali Yacoubi, Rachid Mandry, Mhammed El Allami

DOI: https://doi.org/10.24423/engtrans.2026.3640

Journal: *Engineering Transactions*

ISSN: 0867-888X, e-ISSN: 2450-8071

Publication status: In press

Received: 2025-08-16

Revised: 2026-04-06

Accepted: 2026-04-27

Published pre-proof: 2026-04-30

Please cite this article as:

Jabiri A., Azkour M., Yacoubi A., Mandy R., El Allami M., Numerical Finite Element Modeling of Lamb Wave-Defect Interactions in Bonded Metal Structures: Benchmarking Mode Selection Criteria, *Engineering Transactions*, 2026, https://doi.org/10.24423/engtrans.2026.3640

Numerical Finite Element Modeling of Lamb Wave-Defect Interactions in Bonded Metal Structures: Benchmarking Mode Selection Criteria

Ayoub JABIRI 1)*, Mustapha AZKOUR 2), Abdelali YACOUBI 1), Rachid MANDRY 1), Mhammed EL ALLAMI 1)3)

1) *Laboratoire de Mécanique, Informatique, Électronique et Télécommunications (MIET), Département de Physique Appliquée, Faculté des Sciences et Techniques de Settat (FSTS), Université Hassan Ier*
Route de Casablanca, Km 3.5, BP 539, Settat, Maroc

2) *Laboratoire de Mécanique, Ingénierie et Innovation (LM2I), École Nationale Supérieure d'Électricité et de Mécanique (ENSEM), Université Hassan II*
Route d'El Jadida, Km 7, BP 8118, Oasis, Casablanca, Maroc

3) *Centre Régional des Métiers de l'Éducation et de la Formation (CRMEF)*
Hay Al Farah 2, Rue Taha Hussein, BP 3066, Settat, Maroc

*Corresponding Author e-mail: a.jabiri@uhp.ac.ma

This study investigates the interaction of guided ultrasonic Lamb waves with both internal and surface defects in aluminum/epoxy/aluminum bonded structures. The three-layer assembly consists of two 0.9398 mm-thick aluminum adherends bonded with a 0.25 mm epoxy adhesive core. Three defect configurations are examined: a centered hidden notch (CHN), a single external notch (1EN) located on the upper surface, and two symmetric external notches (2SEN) positioned on opposite faces. Displacement fields acquired from the top surface are processed using a two-dimensional fast Fourier transform (2D-FFT) to decompose the wavefield and identify incident, reflected, and transmitted modes. By calculating acoustic power, we can quantify how energy is distributed across different Lamb modes using specific energy coefficients. This helps pinpoint which modes are best for detecting defects. To figure out the most effective inspection strategy for each type of defect, we carried out a detailed multi-criteria assessment based on energy balance and 13 quantitative indicators. The findings show that both the type and size of a defect can be reliably extracted from these modal energy signatures. Overall, this work supports structural health monitoring (SHM) and nondestructive evaluation (NDE) by offering a rigorous yet practical framework for mode selection that responds well to defects in adhesive-bonded assemblies. The methodology holds significant potential for aerospace and automotive applications, where bond-line integrity is paramount, particularly for ensuring the safety and reliability of critical components such as aircraft structures and automotive chassis. The partial validity of our numerical approach is supported by the experimental study of Santos, whose results are consistent with those obtained in this study.

Keywords: nondestructive testing; Lamb waves; bonded metal structures; finite element method; interaction defect; optimization.

1. Introduction

Structural bonding offers decisive advantages over welding or mechanical fastening: it enables the assembly of dissimilar materials (metals, composites, polymers), ensures uniform stress distribution, enhances fatigue resistance, and eliminates stress concentrations and corrosion risks [1]. These benefits account for its widespread adoption in aerospace, automotive, construction,To capture the wavefield and electronics. However, bonded joints remain susceptible to manufacturing defects as well as to damage that may occur during service, such as cracks, porosity, delamination or localised adhesive failure. Consequently, their early detection and accurate characterisation are essential to ensure the reliability of structures.

In the aerospace and automotive industries, Lamb waves are commonly used for structural inspection, whether in the context of non-destructive testing (NDT) or structural health monitoring (SHM). This type of wave, which propagates in thin plates, has the advantage of traveling long distances with low attenuation while offering high sensitivity to discontinuities, whether internal or superficial.

State of the art. Several research studies have addressed the problem of the interaction between Lamb waves and defects. Rokhlin [2] proposed a theoretical methodology to identify the sensitive modes to inspect the quality of the interface in bonded lap joints. Alleyne and Cawley [3] showed, using the finite element method (FEM) and the two-dimensional Fourier transform (2D-FFT), that the sensitivity of the A0, A1, and S1 modes depends on the frequency-thickness product and the relative depth of the notch. Lowe and Cowley [4] observed that the modes located in the adhesive exhibit better interfacial sensitivity, whereas Lowe *et al.* [5] demonstrated that the symmetric modes, particularly S0, are the most sensitive to variations in the bonded area. Seifried *et al.* [6] highlighted the lower attenuation in regions predominantly composed of aluminum.

Dispersion curves were exploited to highlights the local ultrasonic energy in three-layer structures [7] and relate its distribution to interlayer contact quality. Santos and Perdigão [8] employed leaky Lamb waves to quantify lap joint defects and formulated an empirical correlation between amplitude and defect size. Kumar *et al.* [9] related the frequency shift and the interfacial degradation. Benmeddour [10] demonstrated acoustic reciprocity in symmetric configurations, but pointed out the limitations of mode conversion in asymmetric cases. Birgani *et al.* [11] highlighted the least attenuated modes in metal-adhesive-metal assemblies. Controlled-adhesion samples were validated [12], and the adhesive's impact on energy absorption and modal propagation was confirmed [13]. Modal selection (mode 11 at 3.85 MHz) was employed to accurately pinpoint disbonds in multi-layer assemblies [14]. The symmetric S0 mode has been widely adopted because it shows a stronger response than A0 to epoxy layer thickness variations at low frequencies [15, 16].

Numerical methods have seen notable progress. The finite element method (FEM) provides a robust framework for simulating the interaction between waves and defects [3, 17].

The semi-analytical finite element method (SAFEM), on the other hand, enables efficient calculation of dispersion curves in complex waveguides, including for structures with varying degrees of anisotropy [18,19,20,21]. Recently, the spectral collocation method has also been used for calculating dispersion curves [22,23]. Recent studies combine numerical and experimental techniques [24]. On the signal processing side, 2D-FFT is essential to decompose displacement fields into the wave number frequency domain to separate incident, reflected, and transmitted modes [25, 26]. Welch's periodogram [26] and continuous wavelet transform [27] have been developed for non-stationary signals. The study by Morvan *et al.* [28] analyzed the reflection of Lamb waves at the free end of a plate, and obtained the energy conversion coefficients using three methods: theoretical, numerical (finite element method), and experimental. Excitation of specific modes by energy-normalized, Hann-windowed theoretical displacements has been successfully implemented [29, 30].

Identified gap. Despite these advances, no systematic, quantitative framework exists for selecting the optimal Lamb mode according to the type and symmetry of the defect to be characterized. The choice of the adapted inspection mode is still largely based on an empirical approach, which compromises both the efficiency and reliability of Lamb wave testing.

Objective and approach. This study proposes a comprehensive benchmarking methodology to determine, for a bonded aluminum-epoxy-aluminum structure, which Lamb mode (A0, S0, A1, or S1) is most sensitive and informative for detecting and characterizing three distinct defect types: a Centered Hidden Notch (CHN), a Single External Notch (1EN), and Two Symmetric External Notches (2SEN). The structure is a 1109 mm long, three-layer plate (0.9398 mm aluminum / 0.25 mm epoxy / 0.9398 mm aluminum). Defects are 1 mm wide with depths ranging from 11.74% to 96.26% of total thickness. An excitation frequency of 300 kHz limits propagating modes to four (A0, S0, A1, S1). Dispersion curves are computed via SAFEM. Extensive FEM simulations (COMSOL Multiphysics®) are conducted with energy-normalized, Hann-windowed modal excitations. Normal displacements on the top surface are processed by 2D-FFT; energy maps in the (k, f) domain are compared with SAFEM wavenumbers to identify incident, reflected, and transmitted modes and possible mode conversions.

Innovation and contributions. Each mode's performance is systematically evaluated against thirteen technical criteria (reflected/transmitted energy, energy conservation, sensitivity to small defects, dispersive behavior, number of reflected/transmitted modes, etc.), grouped into three weighted classes to produce an overall score for each mode-defect pair. This multi-criteria approach establishes an explicit link between defect symmetry and optimal Lamb mode: S1 excels for symmetric defects (CHN, 2SEN), while A1 is best suited for asymmetric defect (1EN). The work provides a reproducible methodological framework for mode optimization and delivers practical NDT recommendations for a priori mode selection based on suspected defect type and size.

Paper outline. The remainder of this paper is organized as follows. Section 2 details the geometric and mechanical properties of the three-layer structure, presents the corresponding dispersion curves, and introduces three defect types (CHN, 1EN, 2SEN) with characteristic sizes ranging from 11.74% to 96.26%. Section 3 addresses Lamb wave generation and signal processing, including dispersion analysis at 300 kHz, normalized displacement fields for the A0, S0, A1, and S1 modes, energy-normalized Hann-windowed excitation, and a 2D-FFT decomposition to identify incident, reflected, and transmitted modes. Section 4 provides a detailed energy-based characterization, describing mode extraction, the calculation of reflection (R) and transmission (T) coefficients, and their variations as functions of defect size for each mode and defect type, thereby verifying energy conservation. Section 5 presents a multi-criteria optimization approach based on 13 criteria grouped into three weighted classes. Finally, Section 6 summarizes the main findings, offers practical recommendations for nondestructive testing and outlines future research directions.

2. MODEL DESCRIPTION AND NUMERICAL SETUP

2.1. Geometry and material properties

The present investigation concerns a three-layer isotropic metal-adhesive structure, as shown in Fig. 1. The wave propagates along the direction of the x-axis.

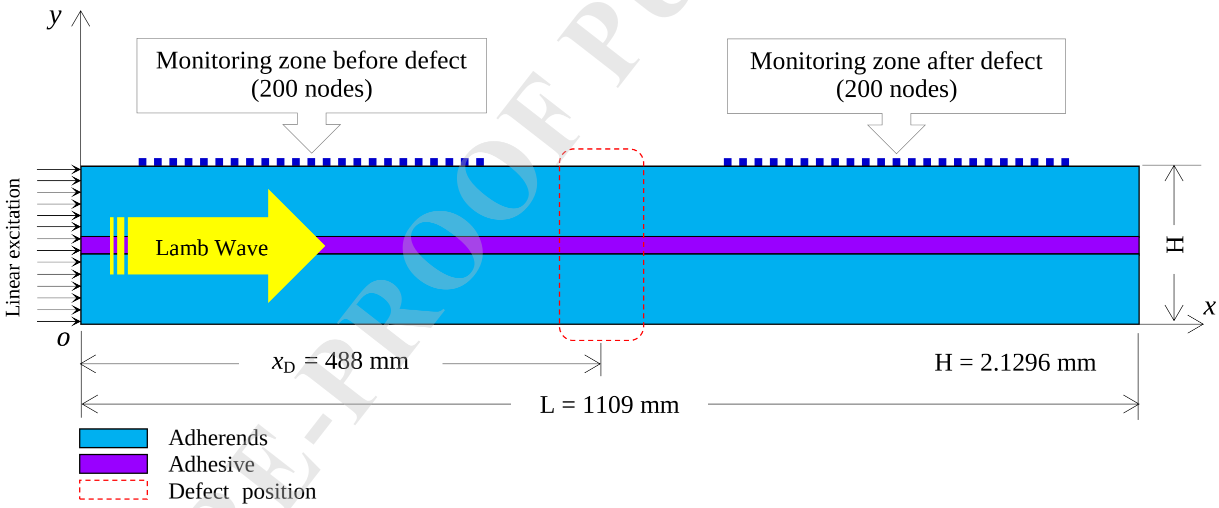

FIG. 1. Numerical schematic of a metal-adhesive structure showing monitoring zones before and after the defect.

The geometric and mechanical properties of each constitutive layer are summarized in Table 1.

TABLE 1. Three-layer structure: Dimensions and material properties.

Layer	Material	E [GPa]	ν	ρ [kg/m^3]	h [mm]	L [mm]
Upper	Aluminum	68.3	0.33	2700	0.9398	1109
Central	Epoxy	0.443	0.39	1106	0.25	1109
Lower	Aluminum	68.3	0.33	2700	0.9398	1109

Note. E : Young's modulus, ν : Poisson ratio, ρ : density, h : thickness, L : length.

Dispersion curves provide a relationship between frequency and wave propagation characteristics, such as wavenumber, phase velocity, group velocity, or wavelength. These curves describe the dispersive behavior of a given structure over a specified frequency range.

In our study, the dispersion curves are computed using the Semi-Analytical Finite Element Method (SAFEM) [15,33,34]. The distinction between symmetric and antisymmetric modes is made by evaluating displacements at the bottom and top surfaces of the three-layer plate. Figure 2 shows the dispersion curves, illustrating the variation of wavenumber, group velocity, and wavelength as functions of frequency.

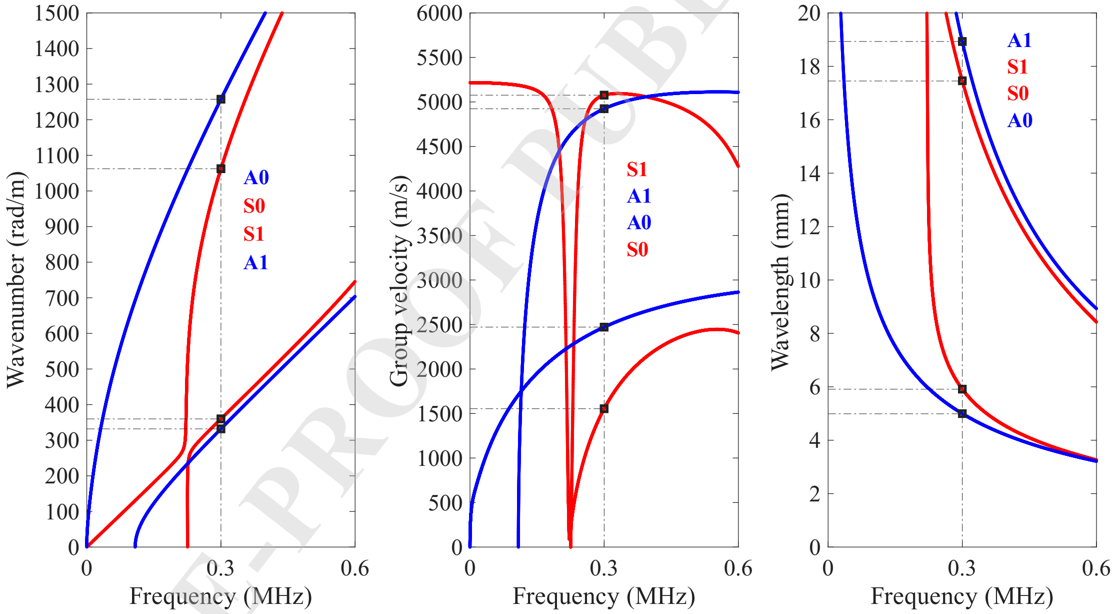

FIG. 2. Dispersion curves of a metal-adhesive structure in the [0–0.6 MHz] frequency range with a 0.3 MHz central excitation frequency.

2.2. Defect configurations

Our objective is to investigate the interaction of Lamb waves with three distinct defect configurations, which are schematically illustrated in Fig. 3 along with their respective size variations.

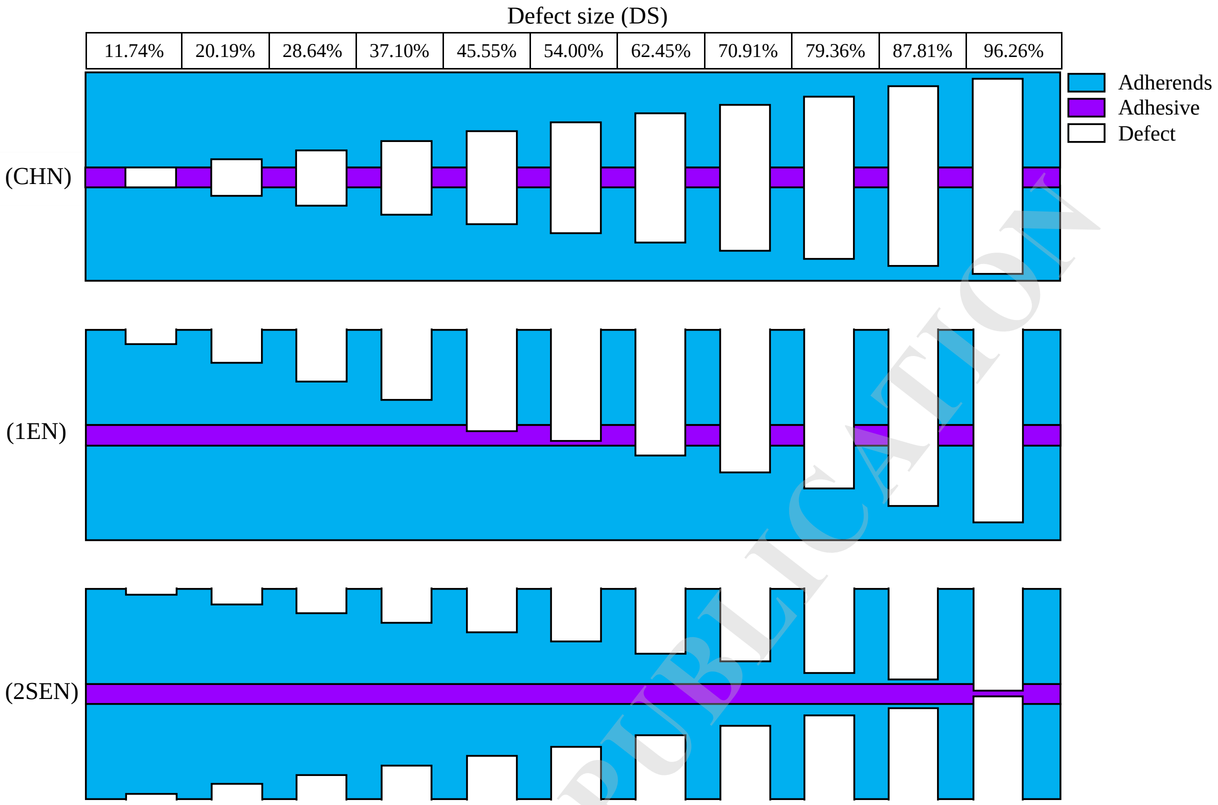

FIG. 3. Classification and size variability of CHN, 1EN, and 2SEN defects.

Defect size exerts a significant influence on Lamb wave propagation by altering both dispersion and attenuation characteristics. The three defect configurations illustrated in Fig. 3 enable a systematic investigation of how the presence and distribution of defects affect the ultrasonic response of the bonded assembly. The structure consists of a three-layer aluminum/epoxy/aluminum sandwich. Defect size (DS) is defined as the ratio of notch depth to total plate thickness and is evaluated at regular intervals ranging from 11.74% to 96.26%. For example, DS = 11.74% corresponds to a minimal defect, whereas DS = 96.26% represents a near-total defect affecting almost the entire cross-section.

Depending on the layers involved, a defect may be classified as delamination or a transverse crack if it extends across multiple layers, or as an inclusion or interfacial detachment if confined to the epoxy layer.

2.3. Meshing and time-step criteria

The schematic (see Fig. 1) illustrates a symmetric sandwich structure composed of two aluminum outer layers adhesively bonded to a central epoxy core. A Lamb wave signal is generated at the left edge of the structure and propagates through a region containing a defect.

To capture the wavefield before and after the defect, two monitoring zones are defined, each containing 200 equally spaced nodes distributed along the propagation direction.

The primary objective is to detect and track Lamb wave propagation within the bonded structure to analyze their interaction with embedded defects. Two monitoring zones, each comprising 200 equidistant measurement points (nodes), are positioned upstream and downstream of the defect. The upstream zone captures both incident and reflected waves, enabling a direct comparison of the wavefield before and after interaction with the discontinuity.

The finite element method (FEM) provides an efficient numerical framework for solving the complex wave equations that govern Lamb wave propagation in structures with various geometries and material configurations. By discretizing the domain into finite elements, the method numerically solves the governing equations to simulate wave propagation behavior. In the present study, a two-dimensional (2D) model is adopted, and the structure is meshed using a triangular mesh.

To ensure numerical stability and physically accurate results, the maximum element size must not exceed one tenth of the smallest propagating wavelength ($\lambda_{\min}$) in the structure. This criterion is expressed as follows [17, 30]:

$$\max(\Delta x, \Delta y) < \frac{\lambda_{\min}}{10} \tag{2.1}$$

To satisfy the spatial discretization requirement, the element sizes Δx and Δy are set between 0.3 mm and 0.5 mm. For numerical stability, the time step Δt must be smaller than the time required for the fastest propagating wave to travel between two adjacent nodes. An upper bound for Δt is given by the following empirical criterion [30, 31]:

$$\Delta t < 0.7\frac{\min(\Delta x, \Delta y)}{V_L} \tag{2.2}$$

To satisfy the stability condition, a time step of $\Delta t = 0.1$ μs is adopted throughout all simulations.

3. GENERATION AND PROCESSING OF LAMB WAVES

Guided Lamb waves are generated by linear ultrasonic excitation at the left edge and propagate through the aluminum/epoxy/aluminum assembly. Upon encountering the defect, the waves undergo partial reflection, scattering, and modifications in frequency content and amplitude. Because the mechanical properties of epoxy differ from those of aluminum, its presence in our structure modifies wave velocity and attenuation, thereby influencing the overall propagation characteristics.

3.1. Dispersive behavior near the excitation frequency

The dispersive behavior of Lamb waves is fundamental for their exploitation in the field of ultrasonic testing and must be rigorously considered in order to optimize the sensitivity and reliability of measurements. The dispersion characteristics depend strongly on both the excitation frequency and the plate thickness. Certain specific applications require the use of low-dispersion modes, such as the S0 mode at low frequency. Dispersion also allows quantitative estimation of residual thickness or the presence of cracks [15]. In order to quantify the dispersive behavior of each mode near the chosen excitation frequency, the derivative of the phase velocity with respect to frequency was calculated, as shown in the figure below.

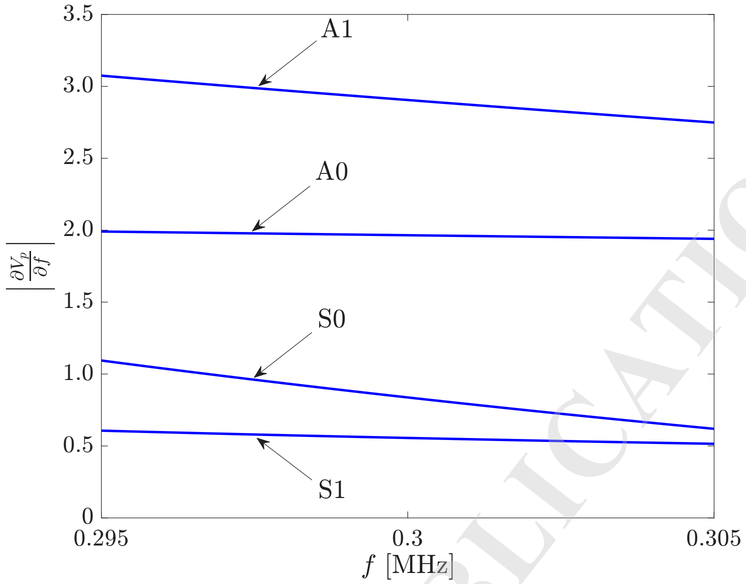

Fig. 4. Phase velocity derivative variation near $f = 0.3$ MHz.

Among the four modes studied, mode A1 exhibits the highest phase velocity derivative, even though it decreases slightly as the frequency increases. Mode A0 remains practically constant across the entire frequency range, meaning it exhibits virtually no dispersion. The S0 mode is characterized by moderate dispersion, with its derivative decreasing slowly as the frequency increases. Mode S1 has the lowest derivative value; it is therefore the least dispersive in this frequency range. Dispersion is a key factor in the analysis of ultrasonic waves within structures: the more significant it is, the faster the signal undergoes distortion. Consequently, the A1 mode is the most dispersive, while the S1 mode is the least dispersive.

3.2. *Normalized mode displacements*

To limit the number of propagating modes, the excitation frequency is kept below the 0.6 MHz threshold, ensuring only four distinct Lamb modes: two antisymmetric (A0 and A1) and two symmetric (S0 and S1). The analytical expressions of the displacement fields employed for linear excitation of the structure are given as follows [27]:

$$\begin{cases} u_x^{(n)} = \left[ik\left(A_n e^{iq_n y} + B_n e^{-iq_n y}\right) + is_n\left(C_n e^{is_n y} - D_n e^{-is_n y}\right)\right] e^{i(kx-\omega t)} \\ u_y^{(n)} = \left[iq_n\left(A_n e^{iq_n y} - B_n e^{-iq_n y}\right) - ik\left(C_n e^{is_n y} + D_n e^{-is_n y}\right)\right] e^{i(kx-\omega t)} \end{cases} \tag{3.1}$$

where A_n, B_n, C_n, and D_n are constants specific to the n^{th} layer, determined from the continuity conditions at the interfaces and the traction-free boundary conditions at the outer surfaces of the aluminum adherends and

$$\begin{cases} q_n = \sqrt{k_{L,n}^2 - k^2} \\ s_n = \sqrt{k_{T,n}^2 - k^2} \\ k_{L,n}^2 = \omega^2 / V_{L,n}^2 \\ k_{T,n}^2 = \omega^2 / V_{T,n}^2 \end{cases} \tag{3.2}$$

In these equations, k denotes the wavenumber. The longitudinal and transverse wave velocities in the n^{th} layer $(n = 1, 2, 3)$ are given by $V_{L,n}$ and $V_{T,n}$, respectively, and ω is the angular frequency. If you normalize the displacement field by the acoustic power—that is, the energy carried by the Lamb waves—you gain a useful understanding of the modal properties. The dimensionless displacement components then come out as:

$$\begin{cases} U_x = u_x / \sqrt{|\mathcal{P}|} \\ U_y = u_y / \sqrt{|\mathcal{P}|} \end{cases} \tag{3.3}$$

$\mathcal{P}$ denotes the energy flux in the propagation direction (x), obtained by integrating over the cross-sectional plane perpendicular to x. The integration domain extends 1 m along the z-axis and spans the full thickness H of the structure along the y-axis. This formulation is expressed mathematically as:

$$\mathcal{P} = -\frac{1}{2} \Re \left(\int_0^H (\mathbf{v}^* \cdot \boldsymbol{\sigma}) \, \mathbf{n} \, dy \right) \tag{3.4}$$

In this formulation, $\boldsymbol{\sigma}$ denotes the stress tensor, $\mathbf{v}$ is the velocity vector, the superscript $*$ indicates complex conjugation, and $\mathbf{n}$ represents the unit normal vector to the differential area element $dz\,dy$.

At an excitation frequency of 0.3 MHz, four propagating Lamb modes are supported: A0, S0, A1, and S1. For each mode, the wavenumber, group velocity, and wavelength are determined using the semi-analytical finite element method (SAFEM) (Fig. 2). The computed values are presented in Table 2.

TABLE 2. Dispersion characteristics of the structure at 300 kHz excitation frequency.

Mode	k [rad/m]	V_g [m/s]	λ [mm]	$\lvert U_y(y = H)\rvert$ [nm]
A0	1258	2471	5.00	0.605
S0	1062	1554	5.91	0.915
A1	331.9	4923	18.93	0.455
S1	359.9	5076	17.46	0.125

Note. k : wavenumber, V_g : group velocity, λ : wavelength, and U_y : normal displacement.

The through-thickness profiles of the normalized displacements at the left cross-section of the metal-adhesive structure are presented below.

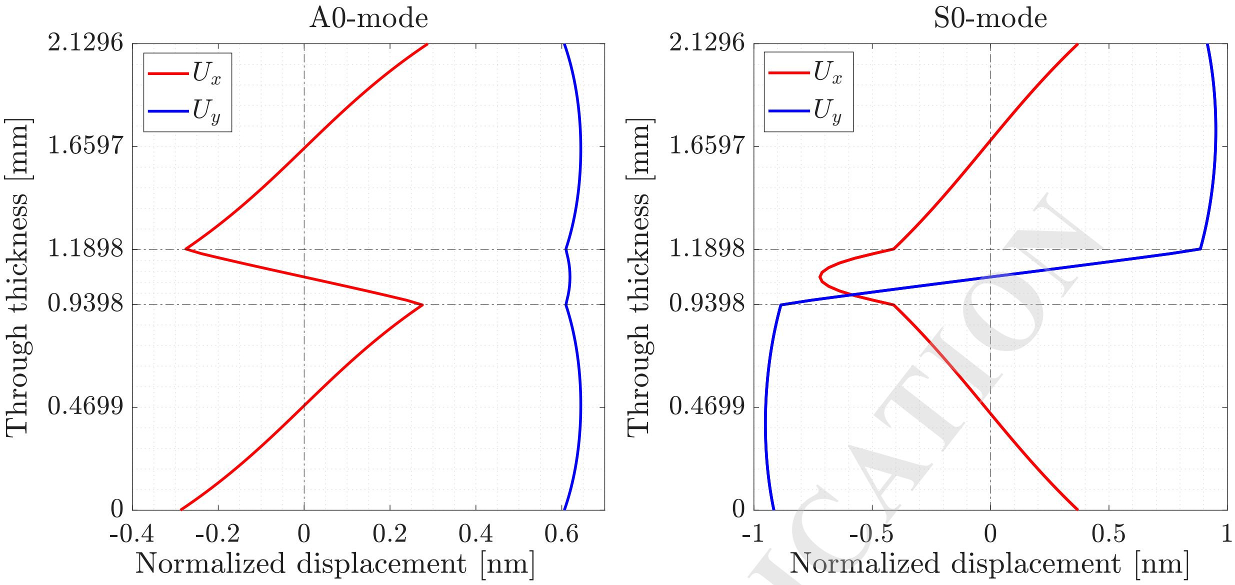

Fig. 5. Normalized displacement profiles across the thickness of a metal-adhesive structure for the A0 and S0 modes.

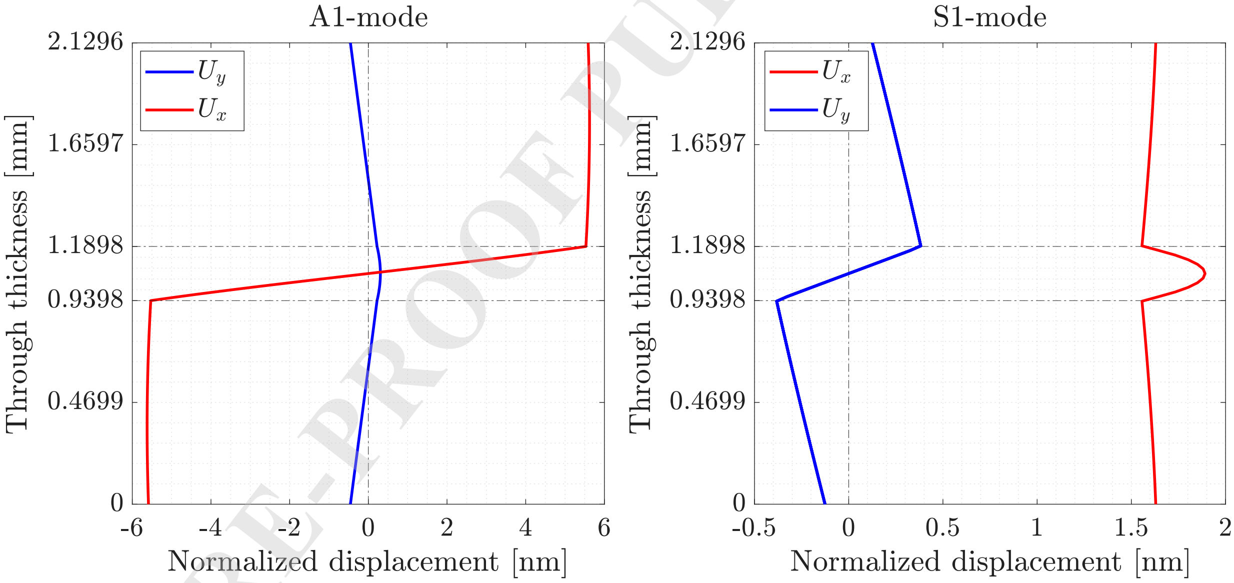

Fig. 6. Normalized displacement profiles across the thickness of a metal-adhesive structure for the A1 and S1 modes.

From Figs. 5 and 6, the following characteristics can be observed for the four modes.

For the A0 mode (Fig. 5), the normal displacement U_y is larger than the longitudinal displacement U_x across all three layers, and U_x vanishes at the center of the structure.

For the S0 mode (Fig. 5), U_y is larger than U_x only in the aluminum layers; it also vanishes at the center of the structure, and a linear behavior of U_y is observed across the entire thickness of the epoxy layer.

Regarding the A1 mode (Fig. 6), the longitudinal displacement U_x now dominates over

U_y, especially in the aluminum layers, and vanishes at the center of the structure. This displacement U_x exhibits a linear variation in the epoxy layer and remains nearly constant in the aluminum layers.

For the S1 mode (Fig. 6), the longitudinal displacement U_x is larger than U_y across the entire thickness of the structure.

3.3. Numerical generation of Lamb waves

To investigate Lamb wave interaction with defects in the metal-adhesive structure, the excitation signal is applied at the left boundary ($x = 0$) over the entire thickness (from $y = 0$ to $y = H$). The structure is excited using both normal and longitudinal displacement components, normalized by the energy flow through the thickness. The excitation consists of a 10-cycle tone burst at 300 kHz, modulated by a Hann window. The corresponding displacement expressions are given below:

$$\begin{cases} E_x(t) = U_x \times \mathcal{H}(t) \\ E_y(t) = U_y \times \mathcal{H}(t) \end{cases} \tag{3.5}$$

The displacement fields are normalized in both directions, with U_x and U_y denoting the normalized displacement components along the x and y axes, respectively. These normalized displacement components are computed analytically, with the Hann window function $\mathcal{H}(t)$ defined as follows [25]:

$$\begin{cases} \mathcal{H}(t) = \dfrac{1-\cos(2\pi t/T_H)}{2}, & t \in [0, T_H] \\ \mathcal{H}(t) = 0, & t \notin [0, T_H] \end{cases} \tag{3.6}$$

In Eq. (3.6), f denotes the excitation frequency, and $T_H = N_c/f$, with N_c being the number of cycles, which is taken equal to 10. The temporal profiles of the excitations, whose analytical expressions are given by Eqs. (3.5) and (3.6), are presented in Fig. 7. It should be noted that the displacement amplitudes are on the order of 10^{-9}. Additionally, a three-dimensional visualization is provided in Fig. 8 to illustrate the linear excitation profiles through the structure's thickness.

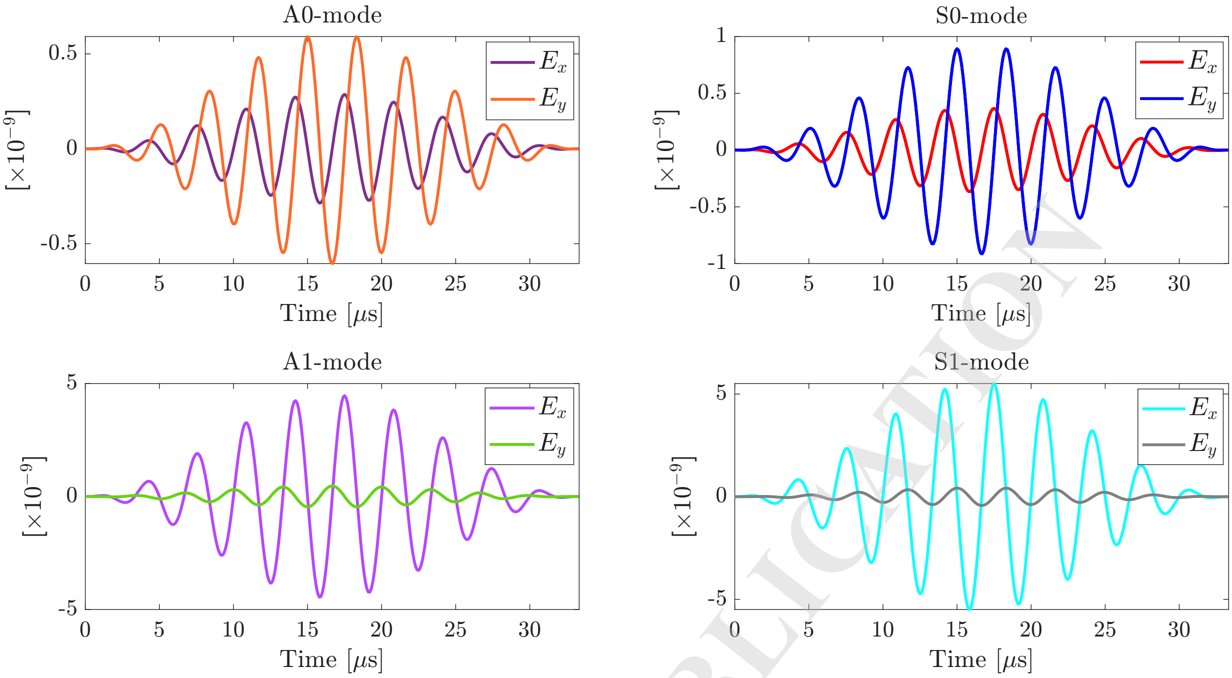

FIG. 7. Transient excitation signal at the top-left corner ($x = 0$, $y = H$).

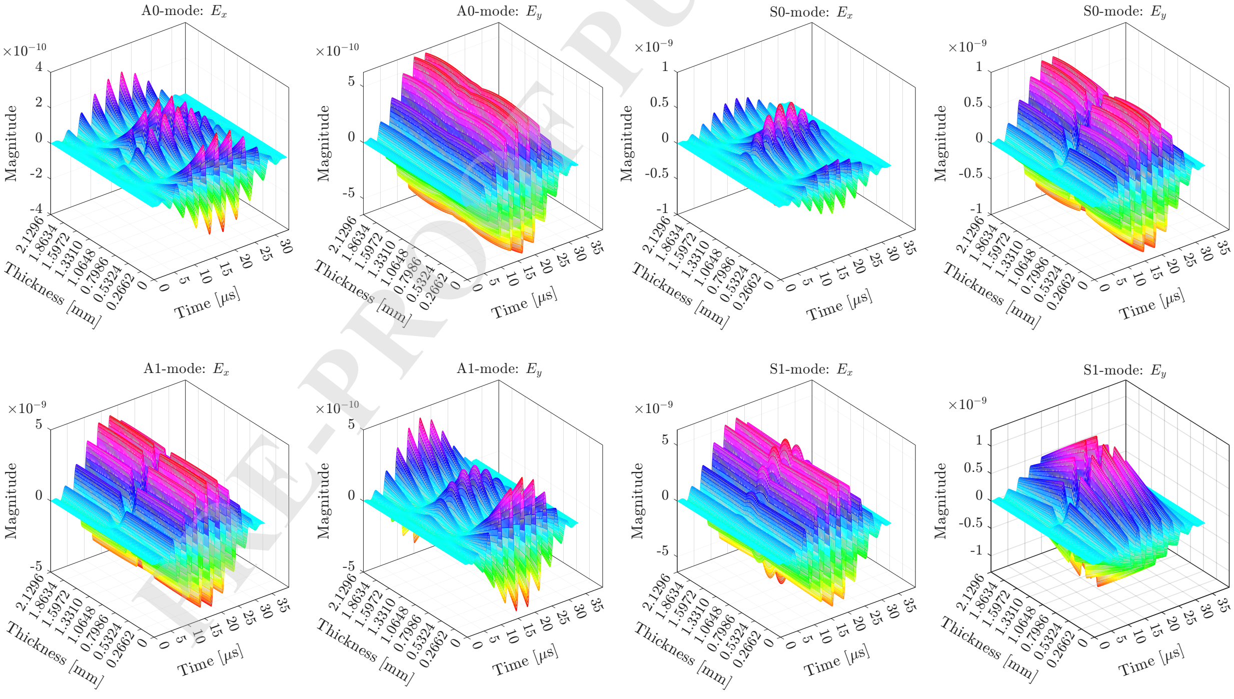

FIG. 8. Through-thickness temporal variations of excitation at $x = 0$ ($0 \leq y \leq H$).

Figure 7 reveals that for the first-order modes (A1 and S1), the excitation component E_y is considerably smaller than the longitudinal component E_x. This disparity is not observed for the fundamental modes (A0 and S0), which are zero-order modes. Moreover, the displacement amplitudes of the first-order modes A1 and S1 are substantially larger than those of the fundamental modes.

3.4. Wavefield decomposition by two-dimensional Fourier transform (2D-FFT) for identification of incident, reflected and transmitted modes

Two sets of 200 measurement points (nodes) are positioned on the top surface ($y = H$) of the structure, covering regions upstream and downstream of the defect to monitor normal displacements, as illustrated earlier in Fig. 1. The first set of 200 nodes, located before the defect between 338 mm and 437.5 mm, are spaced at regular intervals of 0.5 mm. The second set of 200 nodes, placed after the defect between 578 mm and 677.5 mm, follow the same spacing of 0.5 mm. Numerical simulations are conducted using COMSOL Multiphysics software with a time step (Δt) of 0.1 μs and spatial meshing (Δx, Δy) ranging from 0.3 mm to 0.5 mm. The nodes are positioned away from the edges of the structure and the defect to prevent unwanted reflections. Nodes located upstream of the defect capture both incident and reflected wave modes, whereas those downstream record only transmitted modes. All 400 nodes measure normal displacements.

Signal processing based on the two-dimensional fast Fourier transform (2D-FFT) is used to decompose the wavefield and extract relevant features.

Wavenumber-frequency (k–f) domain representations are generated by applying 2D fast Fourier transform (2D-FFT) to the out-of-plane displacement fields obtained from COMSOL simulations. This enables a comparative analysis of the intact and defective structural states. The resulting spectra are shown in Figs. 9 and 10 for the CHN-type defect with DS = 11.74%. This approach allows identification of propagating modes and their interaction with the defect. By comparing the spectra with dispersion curves obtained via the Semi-Analytical Finite Element Method (SAFEM), reflected wave components ($k < 0$) are successfully distinguished from transmitted wave components ($k > 0$) in the wavenumber domain.

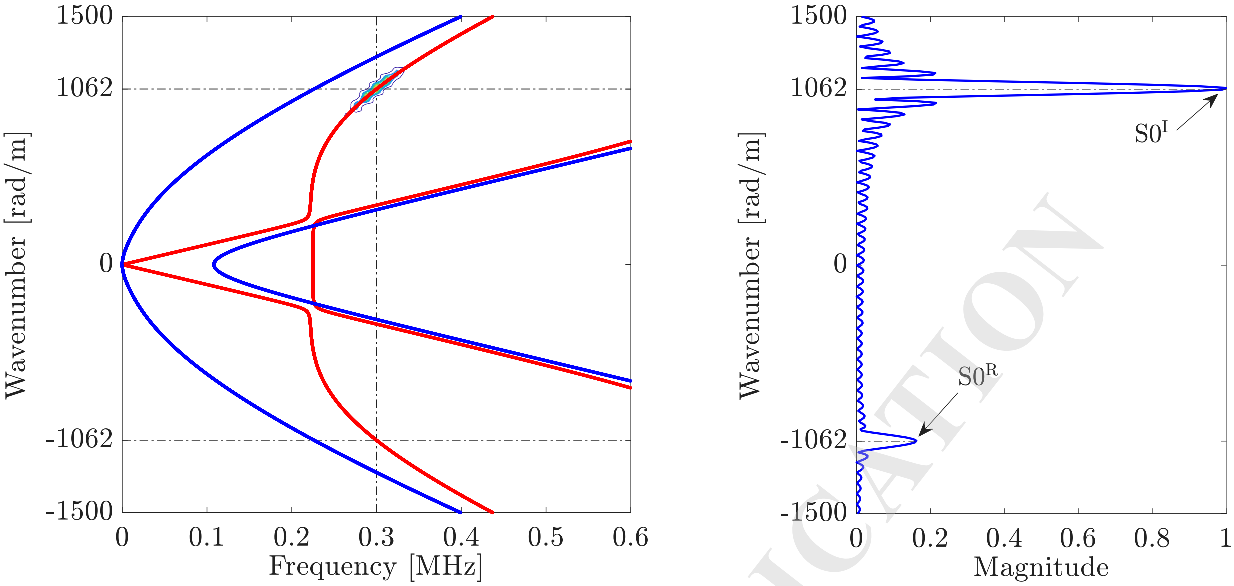

Fig. 9. Correlation between SAFEM-computed wavenumbers and 2D-FFT energy distribution in the (k, f) dual space: Case study of S0 mode excitation before a CHN-type defect (11.74% size).

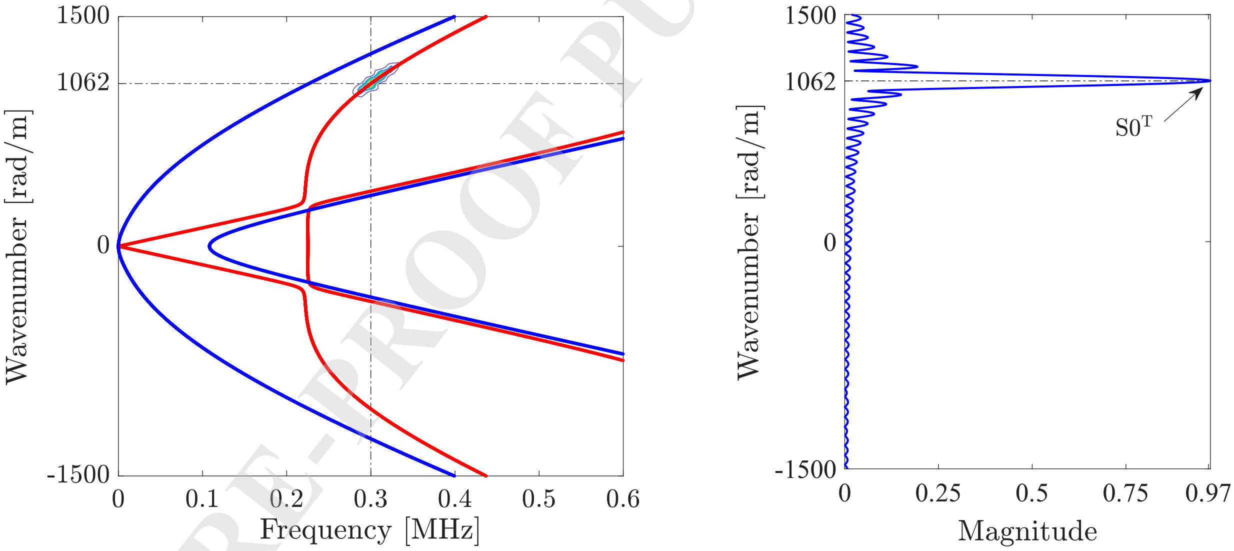

Fig. 10. Correlation between SAFEM-computed wavenumbers and 2D-FFT energy distribution in the (k, f) dual space: Case study of S0 mode excitation after a CHN-type defect (11.74% size).

When the S0 mode is excited (Fig. 9), the incident mode (S0$^{\mathrm{I}}$) has a much larger amplitude than the reflected mode (S0$^{\mathrm{R}}$). However, it is worth noting that the reflected S0 mode (S0$^{\mathrm{R}}$) still retains significant amplitude compared to the incident mode.

Figure 10 shows that the transmitted mode remains unchanged upon leaving the structure in S0 mode and that neither mode conversion for transmission nor reflection is observed.

4. ENERGY-BASED DEFECT CHARACTERIZATION

4.1. Extraction of reflected and transmitted modes

When Lamb modes interact with a defect, they may be reflected or transmitted, either with or without mode conversion. For example, Figs. 11, 12, and 13 provided below are used to extract the modes in the case of a CHN-type defect.

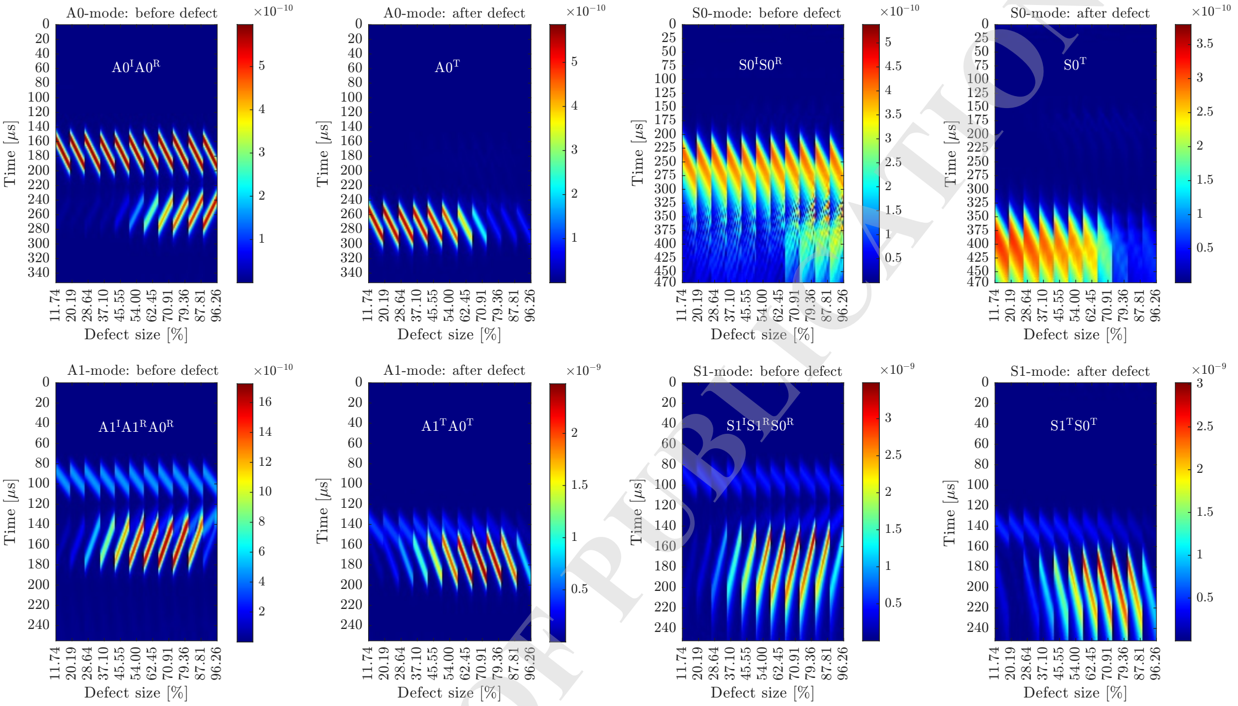

FIG. 11. Normal displacement field for a CHN-type defect.

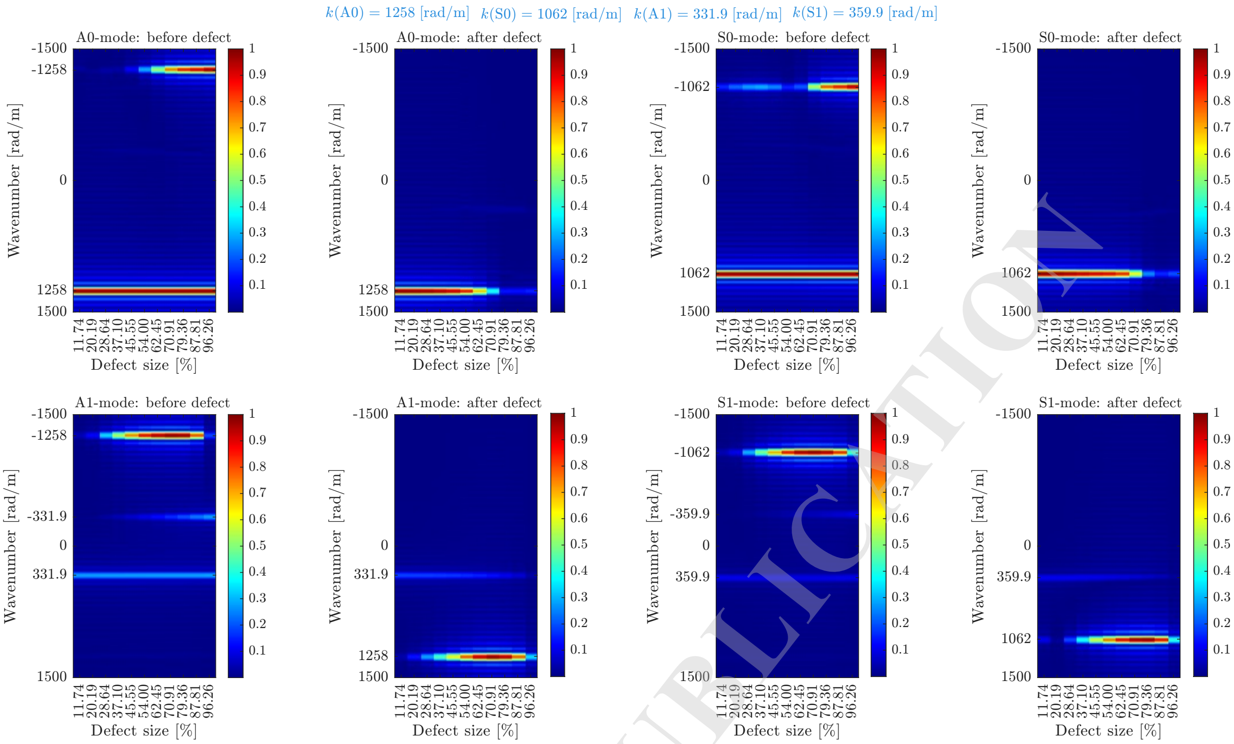

FIG. 12. 2D-FFT spectrum of normal displacements for a CHN-type defect: 3D representation with top view.

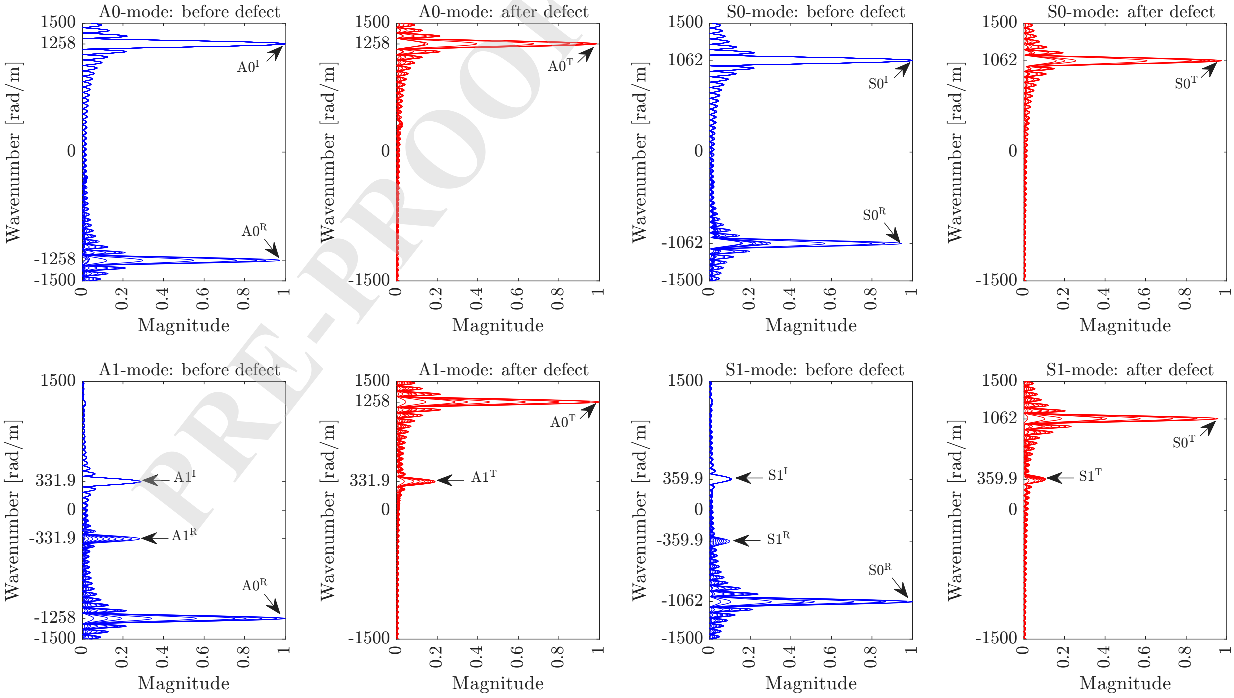

FIG. 13. 2D-FFT spectrum of normal displacements for a CHN-type defect: 2D profile view for all the defect sizes considered.

An important piece of information is reported: during post-processing, it was observed that the first-order modes (A1 and S1) reveal the presence of parasitic modes during excitation, and when the excitation is performed using the A0 or the S0 mode, no parasitic mode is observed. It should also be noted that when excitation is performed using A1 or S1 for a healthy plate (absence of defects), the parasitic mode disappears on the incidence side.

Table 3 records all reflected and transmitted modes for the three configurations of defects considered.

Table 3. Reflected and transmitted modes for symmetric and asymmetric defect configurations.

Defect Configuration	Excited Mode	Reflected Modes			Transmitted Modes		
Symmetric (CHN/2SEN)	A0	A0			A0		
	A1	A1	A0		A1	A0	
	S0	S0			S0		
	S1	S1	S0		S1	S0	
Asymmetric (1EN)	A0	A0	S0		A0	S0	
	A1	A1	A0	S0	A1	A0	S0
	S0	S0	A0		S0	A0	
	S1	S1	S0	A0	S1	S0	A0

Typical Conversion (TC) refers to a change in the modal family after interaction with a defect: A symmetric mode (e.g., S0, S1) converts into an antisymmetric mode (e.g., A0, A1) or vice versa. No Typical Conversion (NTC) indicates the absence of a change in modal family: A symmetric mode remains symmetric (S to S). An antisymmetric mode remains antisymmetric (A to A).

Table 3 compares the mode conversion of Lamb waves during their interaction with symmetric defects (CHN and 2SEN) and an asymmetric defect (1EN). The fundamental result is that symmetric defects, because they preserve the overall geometry of the structure relative to the mid-plane, generate no modal family conversion (NTC). Thus, when an antisymmetric mode like A0 or A1 is excited, only antisymmetric modes are reflected and transmitted; similarly, a symmetric mode (S0, S1) remains purely symmetric after interaction. The fact that modal symmetry stays intact suggests the defect isn't creating any coupling between flexural and extensional movements.

For the asymmetric 1EN defect, though, the loss of symmetry acts like a coupling mechanism, leading to what's called a typical conversion (TC). Take the symmetric S0 mode: when you excite it, not only do you get S0, but you also generate antisymmetric A0 and A1 modes—especially in the reflected signal. On the flip side, sending in an antisymmetric A0 mode creates a symmetric S0 component. This generation of "crossed" modes is a clear sign that the defect is asymmetric. The table also shows that reflection off an asymmetric defect is more complicated, giving rise to more modes than transmission does. That in itself is another clue for identifying the defect type, even without measuring amplitudes.

4.2. Computation of reflection and transmission energy coefficients

As indicated in Eq. 4.1 [10], the reflection and transmission energy coefficients are obtained by dividing the energy of each reflected or transmitted mode by the incident energy:

$$R = \frac{\widetilde{\mathcal{P}}^{\mathrm{R}}_{\mathrm{FEM}}}{\widetilde{\mathcal{P}}^{\mathrm{I}}_{\mathrm{FEM}}} \quad , \quad T = \frac{\widetilde{\mathcal{P}}^{\mathrm{T}}_{\mathrm{FEM}}}{\widetilde{\mathcal{P}}^{\mathrm{I}}_{\mathrm{FEM}}} \quad , \quad \widetilde{\mathcal{P}}^{\mathrm{R}}_{\mathrm{FEM}} + \widetilde{\mathcal{P}}^{\mathrm{T}}_{\mathrm{FEM}} = \widetilde{\mathcal{P}}^{\mathrm{I}}_{\mathrm{FEM}} \tag{4.1}$$

$\widetilde{\mathcal{P}}^{\mathrm{I}}_{\mathrm{FEM}}$, $\widetilde{\mathcal{P}}^{\mathrm{R}}_{\mathrm{FEM}}$, and $\widetilde{\mathcal{P}}^{\mathrm{T}}_{\mathrm{FEM}}$ are the numerically computed mean incident, reflected, and transmitted powers, respectively. The symbols R and T represent the energy reflection and transmission coefficients, respectively. For the case of a CHN-type defect, Figs. 14, 15, and 16 below show qualitatively the results used to calculate these energy coefficients.

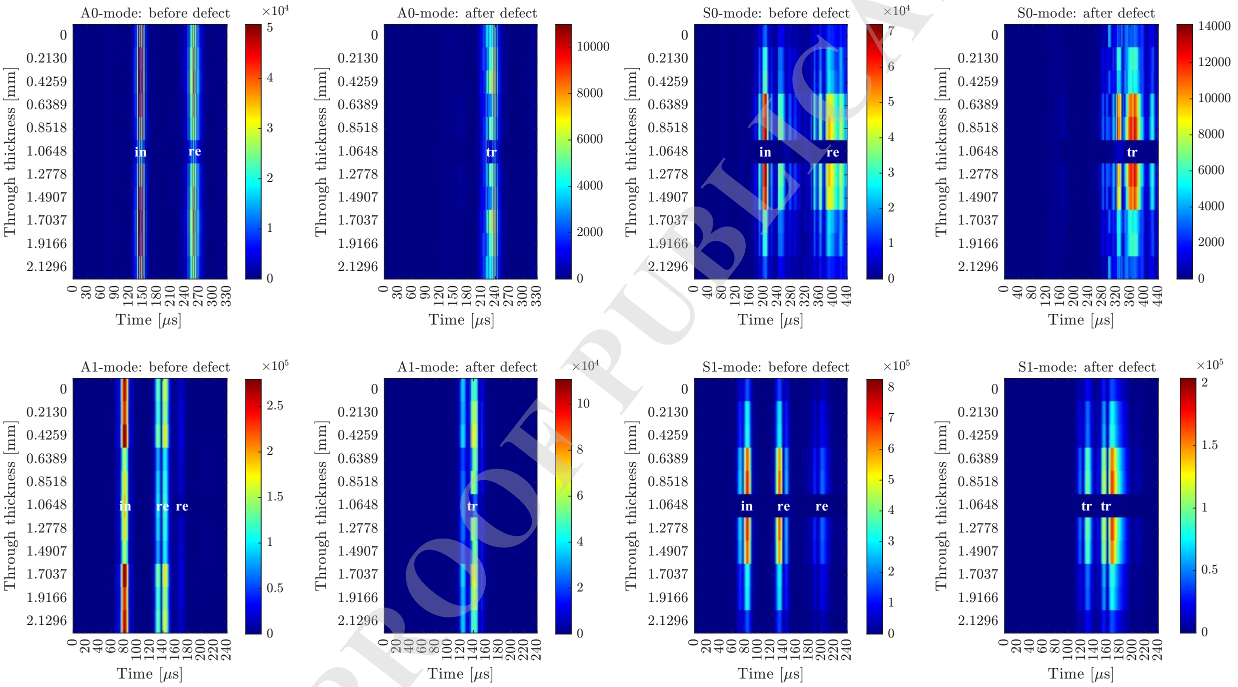

FIG. 14. σ_{xx} stress distribution in the (y, t) domain for a CHN-type defect at maximum size (DS = 96.26%): Upstream ($x = 338$ mm) and downstream ($x = 578$ mm) locations.

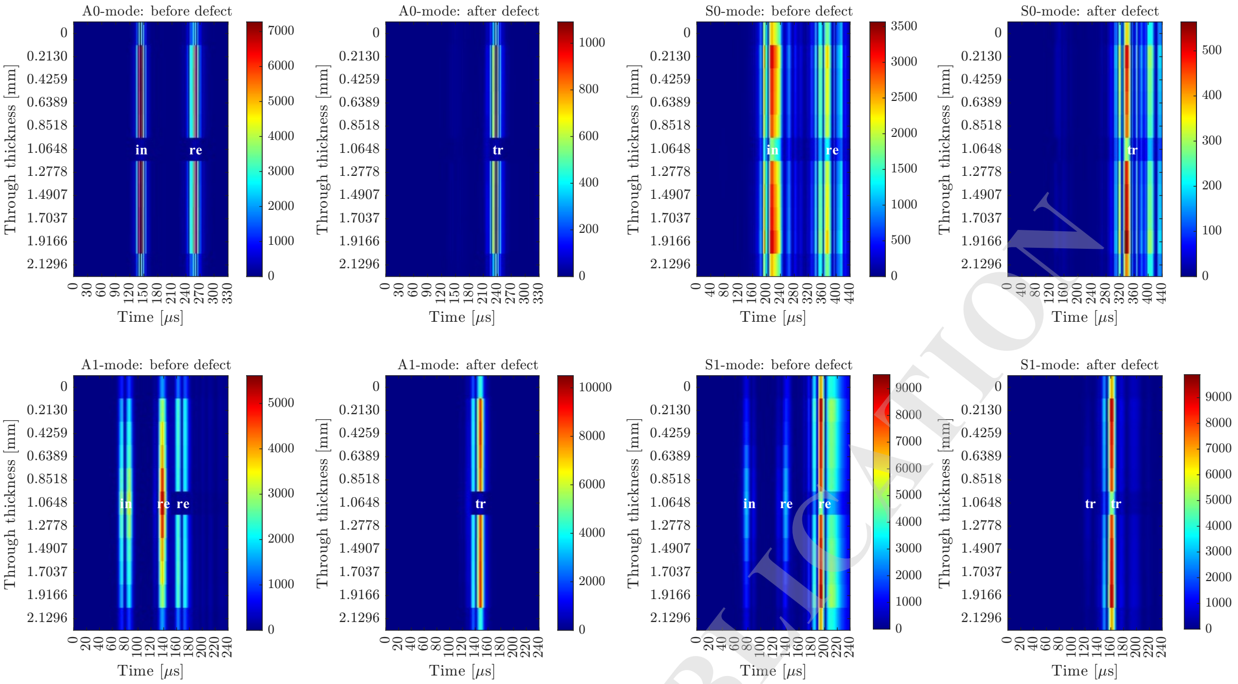

FIG. 15. σ_{xy} stress distribution in the (y, t) domain for a CHN-type defect at maximum size (DS $= 96.26\%$): Upstream ($x = 338$ mm) and downstream ($x = 578$ mm) locations.

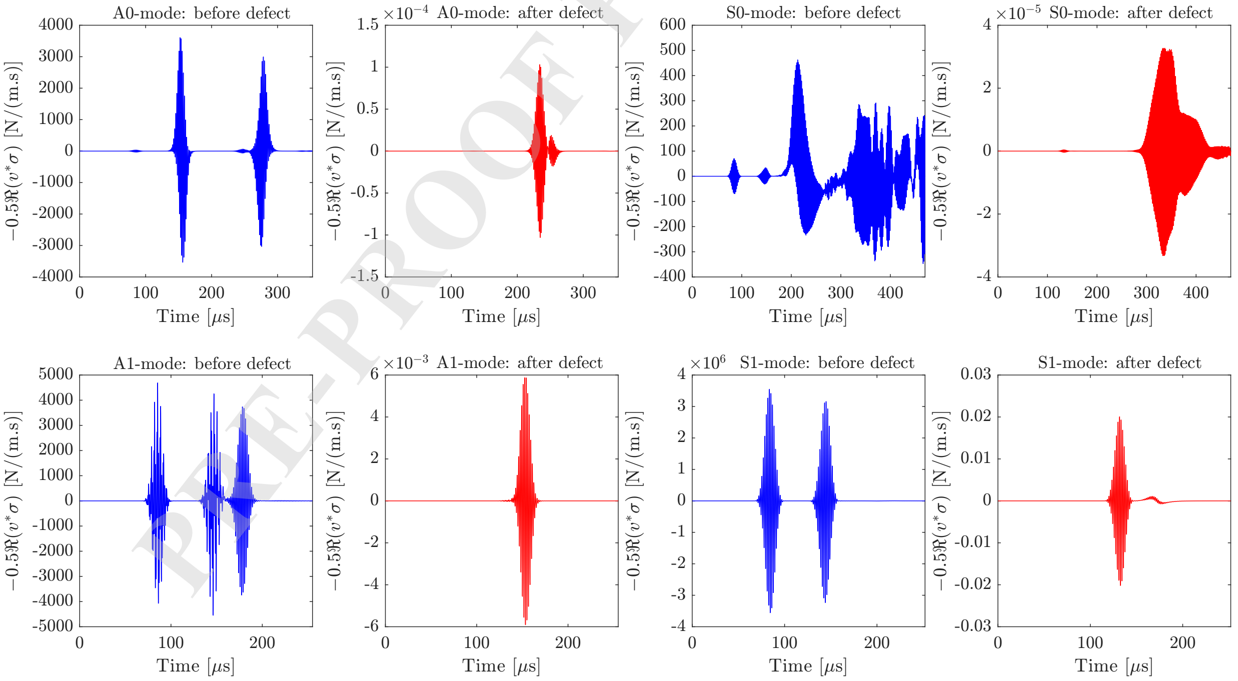

FIG. 16. Transient Poynting vector for maximum-size CHN-type defect configurations.

The severity of the defect directly governs the propagation behavior of Lamb modes, including their sensitivity and energy dissipation. The numerical framework proposed in this study provides access to longitudinal and normal displacement fields (u_x, u_y) and the stress components σ_{xx} and σ_{xy}, from which acoustic power distributions are subsequently computed. The methodology is designed to identify characteristic acoustic signatures of defects, with direct applicability to nondestructive testing (NDT) of adhesive-bonded assemblies. The energy coefficients were determined for each defect type and are presented in Tables 4, 5, and 6.

TABLE 4. Reflection (R) and transmission (T) energy coefficients for a CHN-type defect.

DS [%]	R [%]				T [%]				$R+T$ [%]				Error [%]			
	A0	S0	A1	S1	A0	S0	A1	S1	A0	S0	A1	S1	A0	S0	A1	S1
11.74	1.53	4.39	1.83	1.84	96.60	99.05	99.87	99.19	98.13	103.44	101.70	101.03	-1.87	3.44	1.70	1.03
20.19	2.36	4.74	2.33	5.99	96.04	97.38	99.58	96.99	98.40	102.12	101.91	102.98	-1.60	2.12	1.91	2.98
28.64	3.42	9.11	7.63	11.97	95.42	90.62	96.21	92.45	98.84	99.73	103.84	104.42	-1.16	-0.27	3.84	4.42
37.10	3.55	16.76	14.80	19.37	94.40	83.75	84.95	83.15	97.95	100.51	99.75	102.52	-2.05	0.51	-0.25	2.52
45.55	10.73	25.17	25.28	27.70	89.88	77.99	77.42	73.43	100.60	103.16	102.70	101.13	0.60	3.16	2.70	1.13
54.00	27.39	33.95	40.11	36.56	72.79	64.84	61.15	64.69	100.17	98.79	101.26	101.24	0.17	-1.21	1.26	1.24
62.45	50.90	45.51	54.67	46.03	52.47	56.75	48.29	58.40	103.36	102.26	102.96	104.43	3.36	2.26	2.96	4.43
70.91	71.34	57.15	67.76	55.90	29.33	45.59	33.23	46.36	100.67	102.73	100.99	102.25	0.67	2.73	0.99	2.25
79.36	80.62	69.95	79.77	67.15	16.89	33.95	24.10	33.72	97.51	103.90	103.87	100.87	-2.49	3.90	3.87	0.87
87.81	84.98	84.78	86.94	79.46	13.46	19.12	15.32	17.08	98.44	103.89	102.26	96.54	-1.56	3.89	2.26	-3.46
96.26	92.05	99.17	97.14	95.03	9.16	0.99	3.70	8.31	101.22	100.16	100.84	103.35	1.22	0.16	0.84	3.35

TABLE 5. Reflection (R) and transmission (T) energy coefficients for a 1EN-type defect.

DS [%]	R [%]				T [%]				$R+T$ [%]				Error [%]			
	A0	S0	A1	S1	A0	S0	A1	S1	A0	S0	A1	S1	A0	S0	A1	S1
11.74	3.54	16.06	10.64	8.60	95.49	86.87	92.29	91.00	99.03	102.93	102.93	99.60	-0.97	2.93	2.93	-0.40
20.19	9.33	32.55	25.24	18.11	90.44	70.82	73.27	84.96	99.77	103.37	98.51	103.07	-0.23	3.37	-1.49	3.07
28.64	39.87	51.26	43.44	29.36	61.70	49.18	59.46	73.72	101.56	100.44	102.91	103.08	1.56	0.44	2.91	3.08
37.10	55.07	71.25	62.82	41.95	45.04	30.65	39.37	60.61	100.11	101.90	102.18	102.56	0.11	1.90	2.18	2.56
45.55	55.48	76.35	71.26	51.81	44.12	26.33	31.36	47.17	99.60	102.68	102.62	98.98	-0.40	2.68	2.62	-1.02
54.00	56.98	77.70	71.75	52.16	43.84	25.07	29.89	47.14	100.82	102.77	101.65	99.29	0.82	2.77	1.65	-0.71
62.45	57.08	81.19	73.39	53.51	43.52	22.07	29.80	46.80	100.60	103.26	103.18	100.30	0.60	3.26	3.18	0.30
70.91	57.60	82.25	73.39	58.77	42.44	19.96	29.65	43.87	100.03	102.22	103.04	102.65	0.03	2.22	3.04	2.65
79.36	57.67	86.31	75.87	67.56	40.39	16.59	27.12	36.35	98.05	102.91	103.00	103.91	-1.95	2.91	3.00	3.91
87.81	84.55	89.96	76.33	78.66	18.28	11.77	23.86	24.86	102.83	101.74	100.19	103.53	2.83	1.74	0.19	3.53
96.26	93.37	94.08	85.47	92.52	10.36	9.65	11.45	10.41	103.73	103.73	96.92	102.93	3.73	3.73	-3.08	2.93

Table 6. Reflection (R) and transmission (T) energy coefficients for a 2SEN-type defect.

DS [%]	R [%]				T [%]				$R+T$ [%]				Error [%]			
	A0	S0	A1	S1	A0	S0	A1	S1	A0	S0	A1	S1	A0	S0	A1	S1
11.74	6.18	8.32	6.23	8.95	95.85	94.88	97.28	94.46	102.03	103.20	103.51	103.41	2.03	3.20	3.51	3.41
20.19	6.34	14.62	12.66	15.16	94.01	88.59	91.07	86.45	100.35	103.21	103.74	101.61	0.35	3.21	3.74	1.61
28.64	7.88	22.39	20.25	23.33	91.79	80.32	82.95	78.24	99.67	102.70	103.20	101.56	-0.33	2.70	3.20	1.56
37.10	11.40	30.52	28.77	34.11	87.75	74.01	73.40	68.33	99.15	104.54	102.17	102.44	-0.85	4.54	2.17	2.44
45.55	30.15	40.99	38.03	45.67	71.33	59.40	59.81	57.06	101.48	100.40	97.84	102.74	1.48	0.40	-2.16	2.74
54.00	55.03	50.70	47.92	58.26	47.92	50.13	51.67	43.42	102.95	100.83	99.59	101.68	2.95	0.83	-0.41	1.68
62.45	72.11	61.61	61.71	73.20	30.61	37.02	38.20	30.47	102.72	98.63	99.90	103.67	2.72	-1.37	-0.10	3.67
70.91	78.77	73.55	70.95	81.68	18.20	25.70	31.87	21.02	96.97	99.25	102.82	102.70	-3.03	-0.75	2.82	2.70
79.36	83.32	85.86	83.61	91.00	12.32	16.27	19.56	11.04	95.64	102.13	103.17	102.03	-4.36	2.13	3.17	2.03
87.81	91.38	98.09	98.83	97.71	7.28	2.18	2.15	3.89	98.66	100.28	100.99	101.59	-1.34	0.28	0.99	1.59
96.26	93.86	98.98	99.52	99.31	1.96	0.11	0.12	3.34	95.82	99.10	99.64	102.64	-4.18	-0.90	-0.36	2.64

Tables 4, 5, and 6 all summarize the energy distribution based on defect size (DS). Across the four modes A0, S0, A1, and S1, enlarging the defect size results in a steady increase in the reflection coefficient (R) and a corresponding decline in transmission (T). The sum $R+T$ remains close to 100% in all cases, confirming energy conservation.

Table 4 shows that, for every defect size, the S0 mode reflects more energy than the other modes. At the smallest defect size (DS = 11.74%), the reflected energy for S0 ($R = 4.39\%$) is at least double that of the other modes, which aligns perfectly with the exceptional sensitivity reported by Santos [32]. In the case of an asymmetric single external notch (1EN), the S0 mode again yields the highest reflection coefficient across all defect sizes.

Table 6 presents the same trends for two symmetric external notches (2SEN). However, the S1 mode exhibits greater energy reflection than the other modes for nearly all defect sizes.

The symmetric S0 mode is widely used because it exhibits greater sensitivity to variations in epoxy layer thickness at low frequencies than the A0 mode [15]. This behavior is clearly observed in Table 4 for the smallest defect size (DS = 11.74%), in Table 5 for the defect sizes of 45.55% and 54%, and in Table 6 for the largest defect size (DS = 96.26%).

For a precise and continuous quantification of a defect's size, it is necessary to have energy-based indicators directly proportional to the wave-defect interaction. The reflection (R) and transmission (T) coefficients, defined as the ratios between the reflected/transmitted acoustic powers and the incident power, meet this need. They not only allow verification of energy conservation but also establish an unambiguous relationship between the amplitude of the perturbed waves and the actual dimension of the damage. The objective of this section is therefore to explore, for each Lamb mode (A0, S0, A1, S1) and each defect type (CHN, 1EN, 2SEN), the evolution of the R and T coefficients as a function of the defect size (DS). Figures 17, 18, and 19 present these evolutions and form the basis for the quantitative analysis that follows.

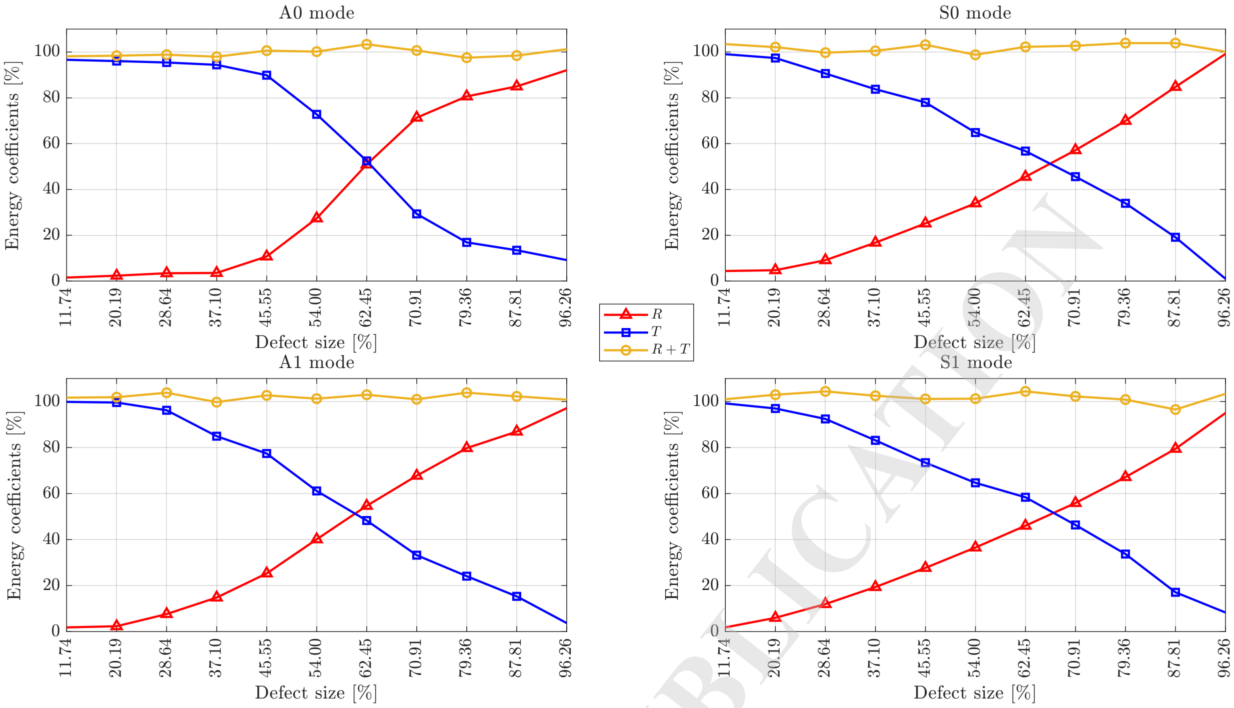

FIG. 17. Energy partitioning into reflected (R) and transmitted (T) components induced by a CHN-type defect.

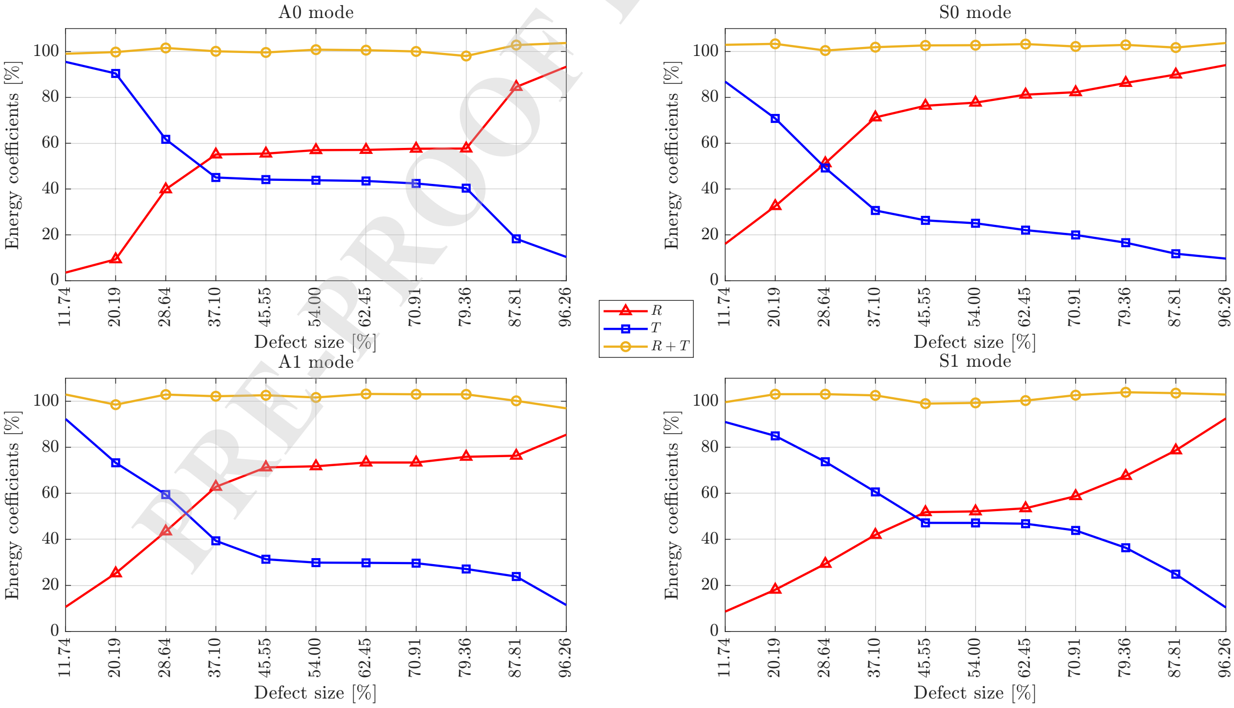

FIG. 18. Energy partitioning into reflected (R) and transmitted (T) components induced by a 1EN-type defect.

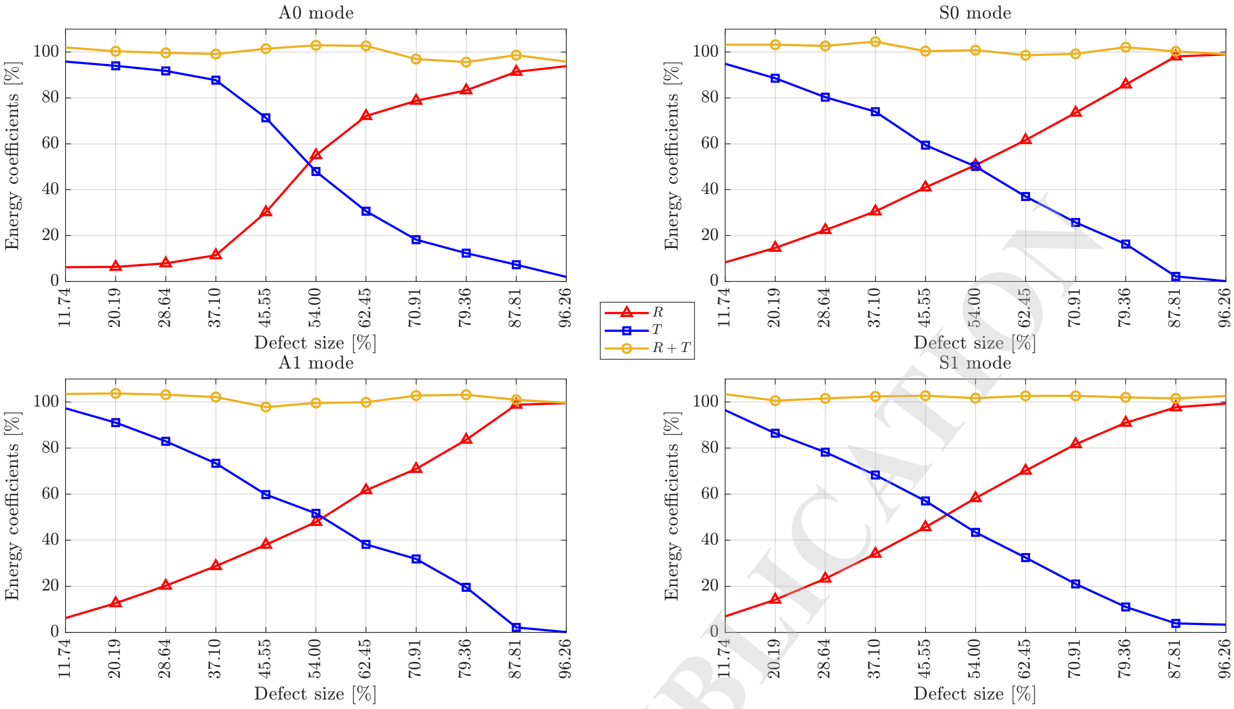

FIG. 19. Energy partitioning into reflected (R) and transmitted (T) components induced by a 2SEN-type defect.

Figures 17, 18, and 19 show the evolution of reflected and transmitted energies as a function of defect size for several Lamb wave modes (A0, S0, A1, S1). In all cases, increasing defect size leads to a monotonic decrease in transmitted energy (T) and a corresponding increase in reflected energy (R). The sum $R + T$ remains consistently close to 100%, confirming that energy conservation is rigorously satisfied throughout the simulations.

Although this general trend holds for all modes, the rate and shape of the transition vary significantly from one mode to another. For small defect sizes, transmission dominates: the wave propagates through the discontinuity with minimal alteration. When the defect size reaches approximately 80–90% of the total thickness, reflected energy becomes dominant. Thus, a small defect acts as a minor perturbation, while a more severe defect behaves as an increasingly effective barrier, reflecting a growing proportion of the incident energy.

This behavior is fully consistent with Lamb wave propagation theory, in which the wave–defect interaction is governed by the ratio of the characteristic defect dimension to the incident wavelength of the interacting mode. All modes examined exhibit this same general tendency, demonstrating that Lamb waves maintain coherent global behavior even in the presence of structural defects. This property can be exploited in nondestructive testing to estimate defect size from reflection and transmission measurements.

5. CRITERIA AND WEIGHTING

Table 7 presents a weighting of the Lamb modes for each defect type based on 13 criteria (see Table 8) to determine the optimal mode. We have to note that the four modes A0, S0, A1, and S1 are ranked according to their satisfaction with respect to each criterion. This satisfaction is assessed using the scores 3, 5, 7, and 9. Classes A, B, and C also differ in terms of importance.

Table 7. Criteria and weighting for optimal mode selection.

DEFECT	MODES	CLASS A [×10]							CLASS B [×7]			CLASS C [×4]			TOTAL
		Cr1	Cr2	Cr3	Cr4	Cr5	Cr6	Cr7	Cr8	Cr9	Cr10	Cr11	Cr12	Cr13	
CHN	A0	3	10	3	3	7	3	5	5	5	5	10	10	10	565
	S0	7	5	5	10	5	5	3	7	3	3	10	10	10	611
	A1	5	7	7	5	10	10	7	3	7	7	7	7	7	713
	S1	10	3	10	7	3	7	10	10	10	10	7	7	7	794
1EN	A0	5	10	3	3	5	3	5	5	5	7	10	7	7	555
	S0	10	3	5	10	10	5	3	7	3	5	10	7	7	661
	A1	7	7	7	7	7	10	7	3	7	10	7	5	5	728
	S1	3	5	10	5	3	7	10	10	10	10	5	5	5	700
2SEN	A0	3	10	3	3	7	3	5	5	5	5	10	10	10	565
	S0	7	3	10	7	5	5	3	7	3	3	10	10	10	611
	A1	5	5	5	5	3	10	7	3	7	7	7	7	7	603
	S1	10	7	7	10	10	7	10	10	10	10	7	7	7	904

The criteria (see Table 8) are grouped into classes, each of which is assigned a weighting score. This grouping reflects the fact that certain criteria may be strongly correlated.

Table 7 presents the central result of the multi-criteria optimization approach proposed in our paper: the performance score of each Lamb mode (A0, S0, A1, S1) for inspecting each defect type (CHN, 1EN, 2SEN). This score is calculated by evaluating each mode against 13 technical criteria (grouped into three weighted classes: A, B, and C). The table reveals a fundamental conclusion: the defect's symmetry dictates the choice of the optimal mode.

For symmetric defects (CHN and 2SEN), the S1 mode achieves the highest scores (**794** and **904**, respectively). For the asymmetric defect (1EN), the antisymmetric mode A1 performs best (score of **728**). It is also observed that the fundamental S0 mode achieves respectable and balanced scores for all defect types (between **611** and **661**), making it an excellent candidate for preliminary screening, thereby confirming Santos' experimental findings. Finally, the A0 mode is systematically the lowest-ranked, particularly for all defects (between **555** and **565**), rendering it unsuitable for this type of configuration.

TABLE 8. Summary of the 13 criteria used for mode optimization.

Criteria	Explanation
Cr1	Reflected energy scale (R).
Cr2	Error arising from the law of conservation of energy.
Cr3	Slope and shape of the reflected energy curve.
Cr4	Sensitivity to small defects.
Cr5	Energy balance point: $R = T = 50\%$.
Cr6	Penetration.
Cr7	Attenuation.
Cr8	Dispersive behavior.
Cr9	Wave overlap.
Cr10	Emergence of parasitic modes.
Cr11	Magnitudes of the reflection and transmission signals relative to the incident signal under mode conversion.
Cr12	Number of reflected modes (NRM).
Cr13	Number of transmitted modes (NTM).

6. CONCLUSION

This study presents a numerical investigation of Lamb wave interactions with three distinct defect types in an aluminum/epoxy/aluminum bonded structure, namely, a centered hidden notch (CHN), a single external notch (1EN), and two symmetric external notches (2SEN) using COMSOL Multiphysics simulations combined with a multi-criteria optimization approach for defect detection and characterization. For each defect type, the most suitable inspection mode was determined by looking at 13 different criteria. The same analysis also helped figure out the type of defect and how big it was. It's worth noting that the defect sizes observed ranged from 11.74% to 96.26% of the structure's overall thickness.

The study relies on three main approaches. First, there's dispersion analysis, which looks for Lamb wave modes that can propagate near a chosen excitation frequency. Second, defect characterization is used to figure out whether a defect is symmetric or asymmetric and to estimate its size based on how the waves interact with it. Third, energy balance and optimization are crucial: this step employs 13 distinct criteria, such as mode sensitivity and energy reflection or transmission coefficients, to select the most suitable Lamb mode for each defect type.

Once the dispersion curves are calculated and all the propagating modes at the selected frequency are identified, the energy balance is set up. Then, the modes are ranked and optimized according to those 13 criteria. The findings clearly link defect symmetry to the choice of the optimal mode. For defects that are symmetric about the structure's middle plane (such as CHN and 2SEN), the symmetric S1 mode works best for both detection and sizing. On the other hand, for the antisymmetric defect (1EN), the antisymmetric A1 mode turns out to be the best choice. This approach performs optimally for antisymmetric defects. One interesting takeaway is that the Lamb S0 mode turns out to be a solid choice for inspecting bonded structures, no matter what kind of defect is present. The results also suggest that, overall, Lamb modes are better at picking up external defects than internal ones. What's more, the S0 mode is especially sensitive to damage inside the adhesive layer—something the A0 mode just doesn't offer.

This study helps us better understand how Lamb waves interact with defects and offers a clear, step-by-step way to choose the right mode based on whether the defect is symmetric or not. It also lays the groundwork for real-world testing and practical use in fields like aerospace, automotive, and civil engineering. The criteria we proposed, along with the energy-based analysis, can serve as handy tools for nondestructive testing and structural health monitoring. They could even be extended to machine learning applications and further experimental work. We used COMSOL simulations to confirm our approach and to help design the experiments.

Looking ahead, we plan to run experimental validations, look into more complex defects and multi-layered structures, and bring in machine learning to automate defect classification. But a few key questions still need answers: How much do changes in material properties like epoxy stiffness affect the results? Could higher-order modes such as A2 or S2 outperform the lower-order ones? And is it possible to trim down the 13 optimization criteria to make them more practical? We aim to tackle these questions in future research.

Nomenclature

Symbol	**Description**
f	frequency
k	wavenumber
V_p	phase velocity
V_g	group velocity
λ	wavelength
u_x	longitudinal displacement
u_y	normal displacement
U_x	normalized u_x
U_y	normalized u_y
σ_{xx}	normal stress
σ_{xy}	shear stress
$\widetilde{\mathcal{P}}^{\mathrm{I}}_{\mathrm{FEM}}$	numerically calculated mean incident power
$\widetilde{\mathcal{P}}^{\mathrm{R}}_{\mathrm{FEM}}$	numerically calculated mean reflected power
$\widetilde{\mathcal{P}}^{\mathrm{T}}_{\mathrm{FEM}}$	numerically calculated mean transmitted power
R	reflection coefficient
T	transmission coefficient
E_x	x-directional excitation
E_y	y-directional excitation
$\mathcal{H}$	Hann window function
$\Delta x, \Delta y$	spatial discretization
Δt	time step
N_c	number of cycles
T_H	Hann period
$\lambda_{\min}$	minimum wavelength
V_L	longitudinal velocity
V_T	transverse velocity
$\mathcal{P}$	acoustic power
H	total thickness of the structure
$\Re$	real part
t	time
μs	microsecond
i	complex unit
$\mathbf{v}$	velocity vector
$\boldsymbol{\sigma}$	stress tensor
$dz\,dy$	cross-sectional area
kHz, MHz	kilohertz, megahertz

Acronyms and abbreviations

Acronym	**Description**
DS	defect size
CHN	centered hidden notch
1EN	single external notch
2SEN	two symmetric external notches
NRM	number of reflected modes
NTM	number of transmitted modes
FEM	finite element method
SAFEM	semi-analytical finite element method
2D-FFT	bi-dimensional fast Fourier transform
NDT	nondestructive testing
TC	typical conversion
NTC	no typical conversion
COMSOL	COMputational SOLutions
A0, A1, S0, S1	antisymmetric (A0, A1) and symmetric (S0, S1) Lamb modes

Funding

The authors received no financial support for the research, authorship, and publication of this article.

Conflict of interest

The authors declare that there are no known competing financial interests or personal relationships that could influence the work reported in this document.

Authors' contributions

Ayoub Jabiri planned the scheme and initiated the project; Mustapha Azkour developed the mathematical modeling and examined the theory validation; Abdelali Yacoubi analyzed the numerical results; Rachid Mandry and Mhammed El Allami directed and supervised the project. The manuscript was written with the contributions of all authors. All authors discussed the results, reviewed, and approved the final version of the manuscript.

References

[1] Adams R.D., and Peppiatt N.A., Stress analysis of adhesive-bonded lap joints, *Journal of Strain Analysis*, **9**(3), pp. 185-196, 1974, https://doi.org/10.1243/03093247v093185.

[2] Rokhlin S.I., Lamb wave interaction with lap-shear adhesive joints: theory and experiment, *The Journal of the Acoustical Society of America*, **89**(6), pp. 2758-2765, 1991, https://doi.org/10.1121/1.400715.

[3] Alleyne D.N., and Cawley P., The interaction of Lamb waves with defects, *IEEE Transactions on Ultrasonics, Ferroelectrics and Frequency Control*, **39**(3), pp. 381-397, 1992, https://doi.org/10.1109/58.143172.

[4] Lowe M.J.S., and Cowley P., The applicability of plate wave techniques for the inspection of adhesive and diffusion bonded joints, *Journal of Nondestructive Evaluation*, **13**(4), pp. 185-200, 1994, https://doi.org/10.1007/BF00742584.

[5] Lowe M.J.S., Challis R.E., and Chan C.W., The transmission of Lamb waves across adhesively bonded lap joints, *The Journal of the Acoustical Society of America*, **107**(3), pp. 1333-1345, 2000, https://doi.org/10.1121/1.428420.

[6] Seifreid R., Jacobs L.J., and Qu J., Propagation of guided waves in adhesive bonded components, *NDT & E International*, **35**(5), pp. 317-328, 2002, https://doi.org/10.1016/S0963-8695(01)00056-1.

[7] Bougaze B., Sidki M., and Ramdani A., Guided ultrasonic waves in the tri-layer structures. Application to the non destructive ultrasonic testing of the bonding quality of sheets, *The European Physical Journal-Applied Physics*, **32**(3): pp. 207-212, 2005, https://doi.org/10.1051/epjap:2005090.

[8] Santos M., and Perdigão J., Leaky Lamb waves for the detection and sizing of defects in bonded aluminum lap joints, *NDT & E International*, **38**(7), pp. 561-568, 2005, https://doi.org/10.1016/j.ndteint.2005.02.004.

[9] Kumar R.L.V., Bhat M.R., and Murthy C.R.L., Some studies on evaluation of degradation in composite adhesive joints using ultrasonic techniques, *Ultrasonics*, **53**(6), pp. 1150-1162, 2005, https://doi.org/10.1016/j.ultras.2013.01.014.

[10] Benmeddour F., Étude expérimentale et numérique de l'interaction des ondes de Lamb en présence d'endommagements dans des structures d'aluminium, Ph.D. thesis, 2006, https://theses.fr/114528330.

[11] Birgani P.T., Sodagar S., and Shishesaz M., Generation of low-attenuation Lamb wave modes in three-layer adhesive joints, *International Journal of Acoustics and Vibration*, **22**(1), pp. 51-57, 2017, https://doi.org/10.20855/ijav.2017.22.1450.

[12] Galy J., Moysan J., El-mahi A., Ylla N., and Massacret N., Controlled reduced-strength epoxy-aluminum joints validated by ultrasonic and mechanical measurements, *International Journal of Adhesion and Adhesives*, **72**, pp. 139-146, 2017, https://doi.org/10.1016/j.ijadhadh.2016.10.013.

[13] Mehrabi M., Soorgee M.H., Habibi H., and Kappatos V., A novel application of ultrasonic Lamb waves: studying adhesive effects on the inspection of coating debonding in a three-layer waveguide, *Nondestructive Testing and Evaluation*, **36**(6): pp. 616-636, 2021, https://doi.org/10.1080/10589759.2020.1843653.

[14] Wang K., Liu M., Cao W., Yang W., Su Z., and Cui F., Detection and sizing of disbond in multilayer bonded structure using modally selective guided wave, *Structural Health Monitoring*, **20**(3), pp. 904-916, 2021, https://doi.org/10.1177/1475921719866274.

[15] Azkour M., El Allami M., and Rhimini H., Calculation of the dispersion curves modeling the propagation of ultrasonic Lamb waves in a bonded aluminum/epoxy/aluminum structure using the semi-analytical finite element method, *Engineering Transactions*, **72**(2), pp. 119-143, 2024, https://doi.org/10.24423/EngTrans.3171.2024.

[16] Baudot A., Moysan J., Payan C., Ylla N., Galy J., Verneret B., and Baillard A., Improving Adhesion Strength Analysis by the Combination of Ultrasonic and Mechanical Tests on Single-Lap Joints, *The Journal of Adhesion*, **90**(5-6), pp. 555-568, 2014, https://doi.org/10.1080/00218464.2013.868806.

[17] Taflove A., and Hagness S. C., 2005, *Computational Electrodynamics: The Finite-Difference Time-domain Method* (3rd ed.), Artech House.

[18] Bartoli I., Marzani A., Lanza di scalea F., and Viola E., Modeling wave propagation in damped waveguides of arbitrary cross-section, *Journal of Sound and Vibration*, **295**(3-5), pp. 685-707, 2006, https://doi.org/10.1016/j.jsv.2006.01.021.

[19] Viola E., Marzani A., and Bartoli I., Semi-analytical formulation for guided wave propagation, in Elishakoff I. (Ed.), *Mechanical Vibration: Where do we Stand?*, International Centre for Mechanical Sciences, Vol. 488, pp. 105-121, Springer, Vienna, 2007, https://doi.org/10.1007/978-3-211-70963-4_6.

[20] Ahmad Z.A.B., Vivar-perez J.M., and Gabbert U., Semi-analytical finite element method for modeling of lamb wave propagation, *CEAS Aeronautical Journal*, **4**(1), pp. 21-33, 2013, https://doi.org/10.1007/s13272-012-0056-6.

[21] Priyadarshinee P., Calculation of wave dispersion curves in multilayered composites using semi-analytical finite element method, *The Journal of the Acoustical Society of America*, **146**(4_Supplement), pp. 2949-2950, 2019, https://doi.org/10.1121/1.5137244.

[22] Zitouni I., Rhimini H., and Chouaf A., Modeling the propagation of ultrasonic guided waves in a composite plate by a spectral approximation method, *Engineering Transactions*, **71**(2), pp. 213-227, 2023, https://doi.org/10.24423/EngTrans.3073.20230510.

[23] Zitouni I., Rhimini H., and Chouaf A., A combined Newton–Bisection approach for calculating the dispersion curves in anisotropic multilayered waveguides, *Journal of Vibration Engineering & Technologies*, **12**, pp. 5189-5201, 2023, https://doi.org/10.1007/s42417-023-01191-1.

[24] Heller K., Jacobs L., and Qu J., Characterization of adhesive bond properties using Lamb waves, *NDT & E International*, **33**(8), pp. 555-563, 2000, https://doi.org/10.1016/s0963-8695(00)00022-0.

[25] Oppenheim A.V., and Schafer R.W., 2010, *Discrete-Time Signal Processing* (3rd ed.). Pearson, Chap. 7. ISBN: 978-0-13-198842-2.

[26] Welch P.D., The use of fast Fourier transform for the estimation of power spectra: A method based on time averaging over short, modified periodograms, *IEEE Transactions on Audio and Electroacoustics*, **15**(2), pp. 70-73, 1967, https://doi.org/10.1109/tau.1967.1161901.

[27] Yacoubi A., Jabiri A., Azkour M., Mandry R., and El Allami M., Wavelet analysis of ultrasonic Lamb wave displacements in three-layer adhesive plates: Continuous wavelet transform (CWT) versus the semi-analytical finite element method (SAFEM), *Engineering Transactions*, **72**(2), pp. 203-224, 2024, https://doi.org/10.24423/EngTrans.3207.2024.

[28] Morvan B., Wilkie-Chancellier N., Duflo H., Tinel A., and Duclos J., Lamb wave reflection at the free edge of a plate, *The Journal of the Acoustical Society of America*, **113**(3), pp. 1417-1425, 2003, https://doi.org/10.1121/1.1539521.

[29] Yuan P., Li X., and Zhou S., Finite element simulation on the reflection and transmission of the lamb waves across a micro defect of plates, *Journal of Vibroengineering*, **21**(3), pp. 611-626, 2019, https://doi.org/10.21595/jve.2018.19814.

[30] Terrien N., Osmont D., Royer D., Lepoutre F., and Déom A., A combined finite element and modal decomposition method to study the interaction of Lamb modes with micro-defects, *Ultrasonics*, **46**(1), pp. 74-88, 2007, https://doi.org/10.1016/j.ultras.2006.11.001.

[31] Courant R., Friedrichs K., and Lewy H., Über die partiellen Differenzengleichungen der mathematischen Physik. Mathematische annalen, *Mathematische annalen*, **100**(1), pp. 32-74, 1928, https://doi.org/10.1007/BF01448839.

[32] Santos M., and Santos J., Adhesive single-lap joint evaluation using ultrasound guided waves, *Applied Sciences*, **13**(11), 6523, 2023, https://doi.org/10.3390/app13116523.

[33] Yacoubi A., Jabiri A., and El Allami M. (2022). Semi-Analytical Finite Element (SAFE) method for plotting Lamb waves dispersion curves of an aluminum plate and comparison with Disperse software. *In ITM Web of Conferences* (Vol. 48, p. 02009). EDP Sciences. https://doi.org/10.1051/itmconf/20224802009.

[34] Jabiri A., Yacoubi A., and El Allami M. (2022). Plotting Lamb waves dispersion curves of an aluminum plate by the Semi-Analytical Finite Element (SAFE) method and comparison with analytical curves. *In ITM Web of Conferences* (Vol. 48, p. 02006). EDP Sciences. https://doi.org/10.1051/itmconf/20224802006